Master Thesis

Novel dopant-free carrier selective contacts for c-Si solar cell

Yan Wang

(5530709)

Supervisor: Prof. dr. Olindo Isabella

Dr. Peyman Taheri

Novel dopant-free carrier selective contacts for c-Si solar cell

By

Yan Wang

in partial fulfilment of the requirements for the degree of

Master of Science

in Materials Science and Engineering

at the Delft University of Technology,
to be defended publicly on Thursday November 30, 2023, at 15:00 PM.

Student number: 5530709

Supervisor:	Prof. dr. Olindo Isabella	
	Dr. Peyman Taheri	
Thesis committee:	Prof. dr. Olindo Isabella	TU Delft, PVMD
	Dr. Peyman Taheri	TU Delft, MSE
	Dr. Sten Vollebregt	TU Delft, ECTM

An electronic version of this thesis is available at http://repository.tudelft.nl/

ABSTRACT

The overdependence on the tradition energy source have caused a serious of ecological problems such as the increasing emission of carbon dioxide. To combat this and achieve carbon neutrality, attention has shifted towards sustainable energy, particularly wind, tidal, and solar energy. The solar cell catches significant interest due to its ability to directly convert solar energy into electricity through the photovoltaic (PV) effect. The silicon heterojunction (SHJ) cells got a lot of attention with high efficiency and simple fabrication process. The record efficiency of SHJ solar cell is 26.81% from Longi [1]. The fabrication process for SHJ solar cells involves the use of plasma enhanced chemical vapor deposition (PECVD). However, the use of toxic and flammable gases in the doping process poses safety risks in laboratories. The parasitic absorption introduced by a doped layer, leads to drawbacks in solar cell performance. Consequently, alternative materials like dopant-free carrier selective contacts (CSCs), divided into hole transport layers (HTL) and electron transport layers (ETL), have attracted considerable interest. Transition metal oxides (TMO) and metal fluorides stand out in dopant-free material research.

This study investigates three metal fluorides (LiF, MgF_X, and SrF_X) as ETL in SHJ solar cells. Initially, four plasma treatments (PTP, PT, PTB, and noPT) are examined as interface treatments in combination with LiF as ETL in SHJ solar cells. Results indicate that PTP is the most compatible with LiF, yielding the highest efficiency. Additionally, studying the impact of LiF thickness on cell performance reveals that a 1 nm thickness shows higher V_{oc} and FF, resulting in higher efficiency. Further exploration into the deposition order of transparent conductive oxide (TCO) and LiF highlights that depositing LiF on the rear side preserves passivation properties, ensuring device performance. Investigations into metal electrode contacts on the rear side reveal that a sputtered Ti/Ag contact with LiF provides the best performance due to its no-venting deposition process. On the front side, copper plating proves superior to screen printing due to better-controlled grids and a less aggressive process, benefiting cell performance.

We expand the optimal parameters obtained from previous experiments to MgF_X and SrF_X. We explore the thickness influence on cell performance. The optimal thickness of MgF_X and SrF_X are 1 nm and 4 nm, respectively. Finally, SHJ solar cells integrated with MoO_X as HTL and LiF, MgF_X, and SrF_X as ETL show significant improvement in light response within the 300-600 nm wavelength range. The combination of MgF_X/MoO_X yields the highest efficiency, with the champion device exhibiting 716 mV of V_{oc}, 38.02 mA/cm^2 of J_{sc}, 76% of FF, and 20.69% efficiency, surpassing reported efficiencies within the same cell structure.

Table of contents

LIST OF TABLES

LIST OF FIGURES

LIST OF ACRONYMS AND ABBREVIATIONS

Abbr.	Explanation
PV	photovoltaic
SHJ	silicon heterojunction
PECVD	plasma enhanced chemical vapor deposition
CSCs	carrier selective contacts
HTL	hole transport layer
ETL	electron transport layers
TMO	transition metal oxides
V_{oc}	open circuit voltage [mV]
FF	fill factor [%]
TCO	transparent conductive oxide
J_{sc}	short circuit current density [mA/cm^2]
c-Si	crystalline silicon
a-Si	amorphous silicon
a-Si:H	hydrogenated amorphous Si
SiH_4	silane
PH_3	phosphine
B_2H_6	borane
η	conversion efficiency [%]
(*i*)a-Si:H	intrinsic hydrogenic amorphous silicon
E_v	Top of Valance band energy [eV]
E_c	Bottom of Conduction band energy [eV]
E_g	band gap energy [eV]
R_s	surface recombination rate [m^{-3}s^{-1}]
p_s	concentration of minority charge carriers [m^{-3}]
p_0	concentration of holes in *n*-type material at equilibrium state
S_r	surface recombination velocity [ms^{-1}]
v_{th}	thermal velocity [ms^{-1}]
σ_p	capture cross-sectional area [m^2]
N_{sT}	surface trap density [m^{-3}]
SRH	Shockley-Read-Hall recombination
Cz-Si	Czochralski silicon
FZ	Float zone melting method
TMAH	tetramethylammonium hydroxide
CVD	chemical vapor deposition
PVD	physical vapor deposition
LPCVD	low pressure chemical vapor deposition
ALD	atomic layer deposition
RF	radio-frequency

e-beam	electron beam
ITO	indium doped tin oxide
IWO	indium tungsten oxide
SP	screen printing
UV	ultraviolet
PR	photoresist
SE	spectroscopic ellipsometry
N	refractive index [-]
K	extinction coefficient [-]
IR	integrating sphere
τ_n	minority carrier lifetime for n-type material
τ_p	minority carrier lifetime for p-type material
i-V_{oc}	implied V_{oc} [mV]
i-FF	implied fill factor [%]
τ	lifetime [ms]
ρ_c	contact resistivity [$\Omega \cdot cm^2$]
I-V	current-voltage
P_{max}	peak power [W]
J_0	saturation current density [mA/cm^2]
I_{ph}	photogenerated current [mA]
STC	standard test conditions
QE	quantum efficiency [-]
SR	spectral responsivity
IPCE	photon-electron conversion efficiency [%]
IQE	internal quantum efficiency [-]
EQE	external quantum efficiency [-]
$\psi_{ph,\lambda}$	spectral photon flow [s^{-1}]
$\phi_{ph,\lambda}$	spectral photon flux [m^{-2}s^{-1}]
$pEff.$	pseudo-efficiency [%]
pFF	pseudo-fill-factor [%]
CP	copper plating
XPS	X-ray photoelectron spectroscopy
TEM	transmission electron microscopy

1. Introduction

Conventional fossil fuels, commonly acquired through combustion-based thermal processes, presently stand as the predominant energy source. While their widespread adoption is driven by cost-effectiveness, it's crucial to acknowledge the finite and non-renewable nature of global fossil fuel reserves. The use of these fuels presents challenges, particularly in terms of carbon dioxide emissions during combustion, contributing significantly to global warming. Given the environmental consequences and the finite supply of fossil fuels, there is an increasing urgency for nations to expeditiously shift towards renewable energy sources, thereby reducing dependence on traditional fossil fuels [2].

Renewable resources, such as solar energy, tidal power, wind, and geothermal energy, contribute to sustainable energy [3]. While comprising a small fraction of global energy consumption, renewables are crucial for carbon neutrality. Solar energy, uniquely capable of direct electricity generation through PV devices, minimizes conversion losses compared to other sources like biomass [4]. Since the year of 1839, PV effect was first identified by Alexandre-Edmond Becquere, a French physicist. After that, the PV industry is developing during the latter 200 years [5].

Figure 1.1 provides insights into the annual PV production across various technologies. Throughout the first two decades of the 21st century, the scale of PV production witnessed a notable expansion [6]. During the initial stages, multi-Si, mono-Si, and thin-film technologies, collectively known as the second-generation PV technology, progressed concurrently, despite solar energy not garnering significant attention at that time. By 2015, multi-Si technology had attained dominance, but in the subsequent developmental phases, mono-Si cells emerged as the leading force in PV production.
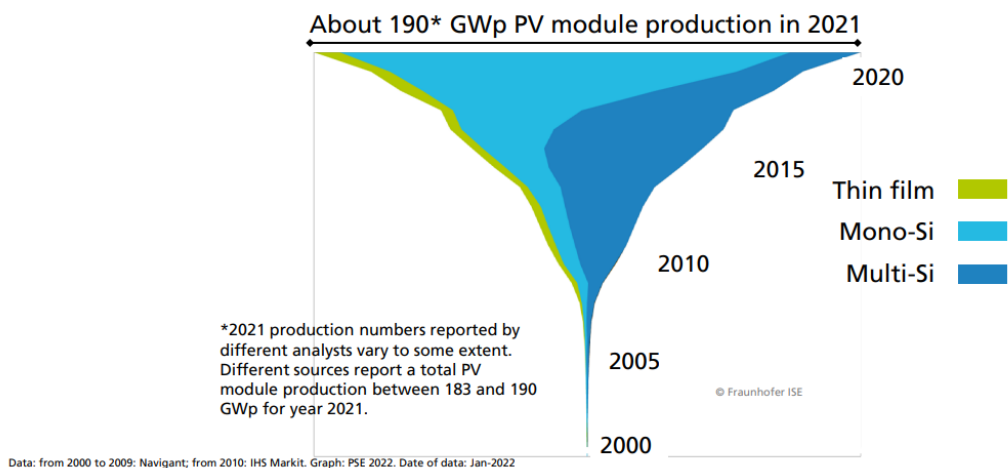
Figure 1.1 PV module production in 2000-2020 [6]

1.1 Background

Silicon heterojunction solar cells employ crystalline silicon (c-Si) and amorphous silicon layers (a-Si), achieving remarkable efficiency and demonstrating adaptability to low-temperature processing. Figure 2 illustrates that crystalline silicon solar cells exhibit promising efficiency in heterojunction solar cells. Front/back SHJ solar cells have attained a record efficiency of 26.81% [7]. Nevertheless, persistent challenges prompt the scientific community to explore possibility for enhancement.
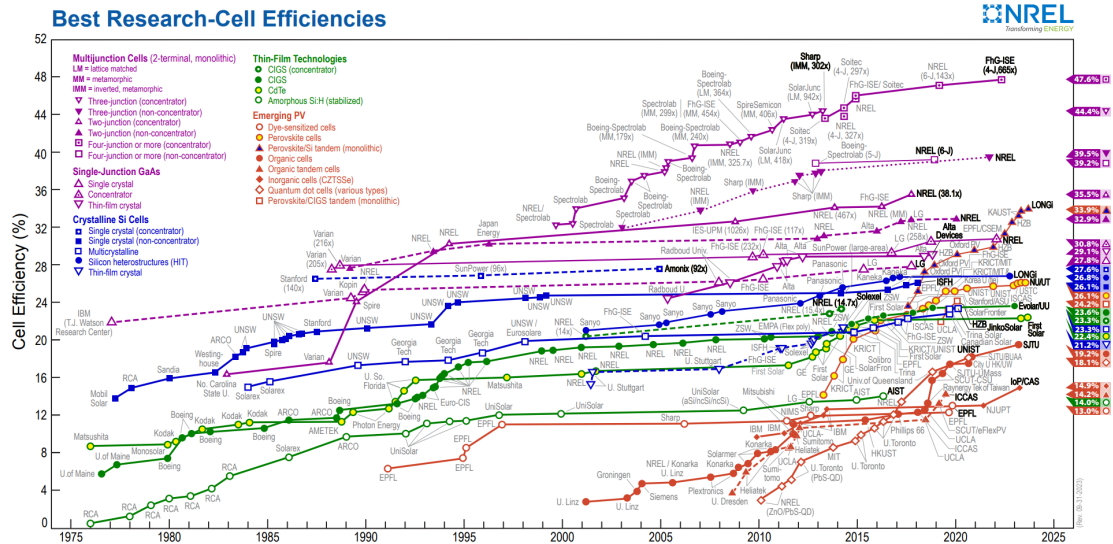
Figure 1.2 Best research-cell efficiency [8]

The PECVD process plays a crucial role in fabricating SHJ solar cells, involving the deposition of intrinsic, p-type, and n-type a-Si:H (hydrogenated amorphous silicon) [9]. However, it's important to note that the precursor gas silane (SiH_4) is flammable. Additionally, the doping gases phosphine (PH_3) and borane (B_2H_6) pose safety concerns due to their toxicity, potential for explosions, and thermodynamic instability [10]. The doped layers also introduce parasitic absorption leading to drawback in device performance [11], [12]. Considering these safety challenges and the pursuit for higher efficiency, there is an imperative need to explore alternative materials to replace the doped layers in SHJ solar cells.

Dopant-free materials with tunable work function and better light response attracted attention to be a sustainable alternative to replace doped layer in SHJ solar cells. The high or low work functions of these dopant-free materials (shown in Figure 1.3) enable the realization of band bending upon contact with c-Si wafer, facilitating selective contact with specific carriers [13], [14]. Realizing dopant-free, carrier-selective passivation contacts for crystalline silicon cells can be achieved through low-temperature processes with fewer sequences. This approach eliminates the use of toxic and flammable gases, aligning with the principles of high efficiency and environmental-friendly. Hence, the substitutional choice involves the utilization of dopant-free carrier selective

contacts.
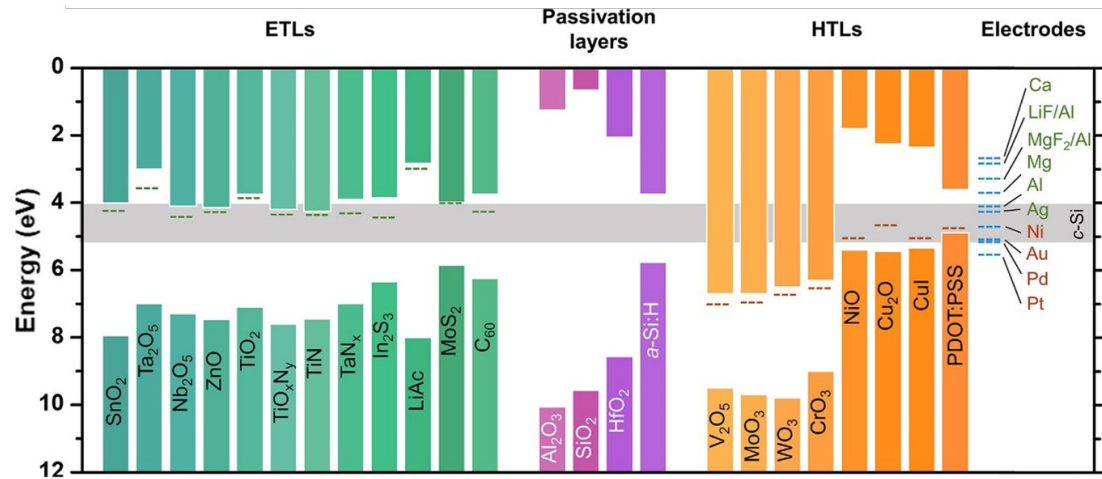
Figure 1.3 Band diagram of CSCs for c-Si cells [14]

Hole transport layer play a crucial role in facilitating the extraction and transportation of positive charge carriers while blocking the flow of electrons. In contrast, electron transport layer exhibits high electron mobility and an affinity for blocking holes, allowing electrons to flow through the layer. The specific role of CSCs as either HTL or ETL depends on their work function and the method of deposition [15]. The reported work based on dopant-free materials are listed in Table 1.1.

Table 1.1 Summary of dopant-free CSCs in previous research

Year	CSCs type	Deposition	Structure	V_{oc} [mV]	J_{sc} [mA/cm^2]	FF [%]	η [%]	Ref.
2015	HTL	Thermal evaporation	MoO_x/i/n-Si	725	38.6	80.4	22.5	[16]
2016	ETL	Thermal evaporation	n-Si/LiF/Al	676	38.9	78.3	20.6	[17]
2016	ETL	Thermal evaporation	n-Si/i/MgF_x/Al	687	37.8	77.3	20.1	[18]
2020	HTL	Thermal evaporation	MoO_x/i/n-Si	734	39.2	81.8	23.5	[19]
2022	HTL	Thermal evaporation	MoO_x/i/n-Si	721	40.2	82.2	23.8	[20]
2023	ETL	Thermal evaporation	n-Si/SrF_x/Al	654	41.9	78.7	21.6	[21]
2017	HTL	ALD	n-Si/i/TiO_x/metal or TCO					[15]
2016	ETL	ALD	n-Si/SiO_2/TiO_x/Al	676	39.6	80.7	21.6	[22]
2016	ETL	ALD	n-Si/TiO_x/Al/Ag	650	39.5	80	20.5	[23]

2018	ETL	ALD	n-Si/i/TiO$_X$/Ca/Al	711	35.1	72.9	18.2	[24]
2019	ETL	ALD	n-Si/TiO$_X$/Al/Ag	695	41.5	80	23.1	[25]
2019	ETL	ALD	n-Si/i/TiO$_X$/Yb/Ag	723	33.8	78.6	19.2	[26]

*i stands for (*i*)a-Si:H

1.2 Research topic

In my thesis, I have chosen three specific metal fluorides for study based on insights gained from the literatures. The optimization of cell structure involves several sequential steps. Initially, four distinct plasma treatments (PTP, PT, PTB, and noPT) are administered on the interface between intrinsic hydrogenated amorphous silicon ((*i*)a-Si:H) and ETL. The gas condition of each treatment is illustrated in Table 1.2. Subsequently, based on the identified optimal plasma treatment, the impact of varying thicknesses of different metal fluorides used as ETL on cell performance will be systematically explored. The cell structure is depicted in Figure 1.4. The investigation aims to determine the optimum thickness for each metal fluoride material. Following this, the order of deposition and the arrangement of front/rear metal contacts will be deliberated to further refine the overall cell configuration.

Table 1.2 Gas condition of treatments

Name of treatments	Gas
PTP	Phosphors, silane, hydrogen
PT	Silane, hydrogen
PTB	Borane, silane, hydrogen, carbon dioxide
noPT	none
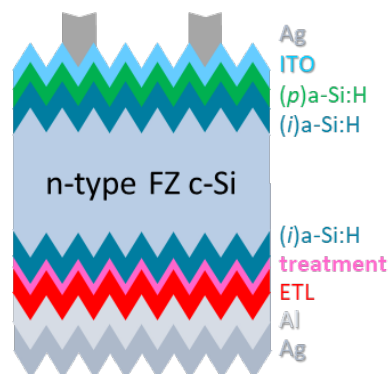
Figure 1.4 Schematic of initial cell structure

In the final phase, a dopant-free solar cell will be fabricated, employing MoO$_x$ as HTL and the optimized thickness of the chosen ETL material. This configuration aims to

enhance the overall efficiency of the solar cell. The fabrication process will be comple-mented by a comprehensive suite of characterization methods to thoroughly assess and understand the resulting device's performance and properties.

2. Physical fundamentals

Chapter 2 are mainly focus on the physical foundations related to solar cells. This chapter is divided into five sections. Starting with an exploration of silicon as the fundamental and pivotal material for solar cells, the chapter progresses to explain the operational principles of solar cells. Subsequently, the dopant materials and silicon heterojunction are illustrated. In the pursuit of enhancing cell efficiency, a detailed examination of loss pathways and recombination mechanisms ensues. The final part is aimed at carrier selective contact that is the central focus of research within this thesis.

2.1 Silicon

Silicon (Si), characterized by an atomic number of 14, is a pervasive element constituting 27.7% of the Earth's crust, as depicted in Figure 2.1 (a). Silicon stands as the second most abundant element. Possessing a face-centered diamond cubic crystal structure with a lattice parameter of 0.543 nm, the crystal structure of Si is illustrated in Figure 2.1 (b). Each silicon atom has four electrons in its outermost orbital and forms covalent bonds by sharing electrons with its nearest neighbor atoms. This arrangement reveals silicon with a stable and complete valence bond structure.
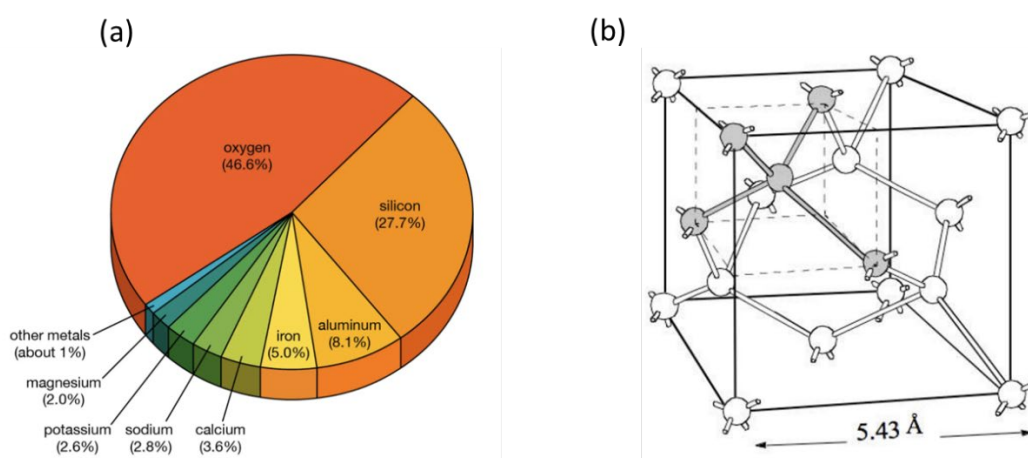
Figure 2.1 (a) The composition of elements in earth crust [27], (b) Silicon crystal structure [28]

The energy bands of the Si crystal are depicted in Figure 2.2. Here, E_v denotes the top edge of the valence band. On the other hand, E_c represents the bottom edge of the conduction band. The separation between E_v and E_c is defined as the band gap energy, denoted as E_g, where $E_g = E_c - E_v$. E_g signifies the energy required for charge carriers to move from the valence band to the conduction band. For crystalline silicon, E_g is measured as 1.12 eV at 300 K [29]. This implies that wavelength of light shorter than 1107nm contributes to the conversion of solar energy in the case of crystal silicon.
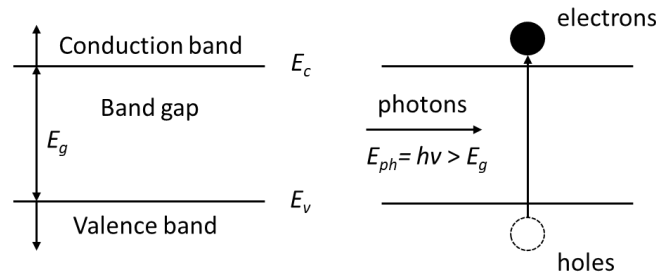
Figure 2.2 The band gap of Si and molecule orbitals

2.2 The working principle of the solar cell

Solar cells are devices that utilize PV effect of semiconductor materials to convert solar energy directly into electricity. Figure 2.3 illustrates the working principle of a solar cell. The PV effect can be divided into three main steps: absorption, separation, and collection processes.
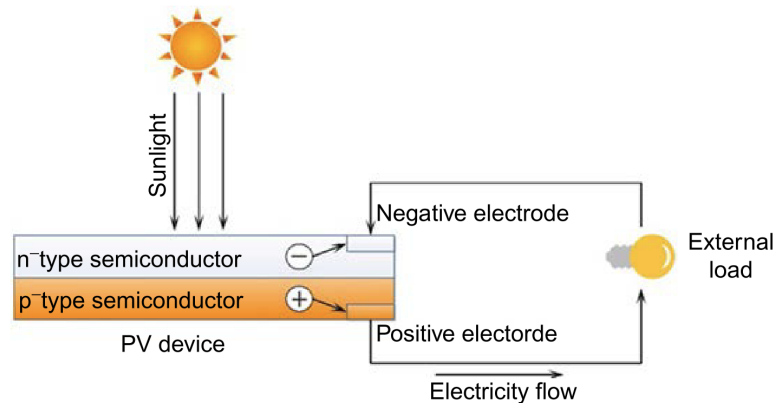
Figure 2.3 The working principle of a PV cell [30]

The initial stage occurs when sunlight strikes the solar cell. Photon absorption takes place only for photons with energy greater than the material's bandgap. Photons with lower energy pass through the material. As a result, electron-hole pairs are generated. The crucial component in c-Si solar cells is the p-n junction. In its presence, the potential recombination of electron-hole pairs is prevented as they are separated by n- and p-type materials, as illustrated in Figure 2.3. Ultimately, the separated electrons and holes migrate to the cathode and anode, respectively, creating an electric current.

2.3 Doped semiconductor

In intrinsic silicon, as depicted in the two-dimensional representation in Figure 2.4 (a), the silicon atom in the middle shares electrons with four surrounding silicon atoms. To achieve n-type silicon, phosphorus as a donor is introduced, providing one free electron as illustrated in Figure 2.4 (b). Conversely, if boron is introduced into silicon, three electrons in the outer valence shell are required to form additional covalent bonds, leaving a hole with a positive charge. Boron, as an impurity atom, acts as an acceptor,

7

leading to *p*-type semiconductor characteristics, as shown in Figure 2.4 (c).
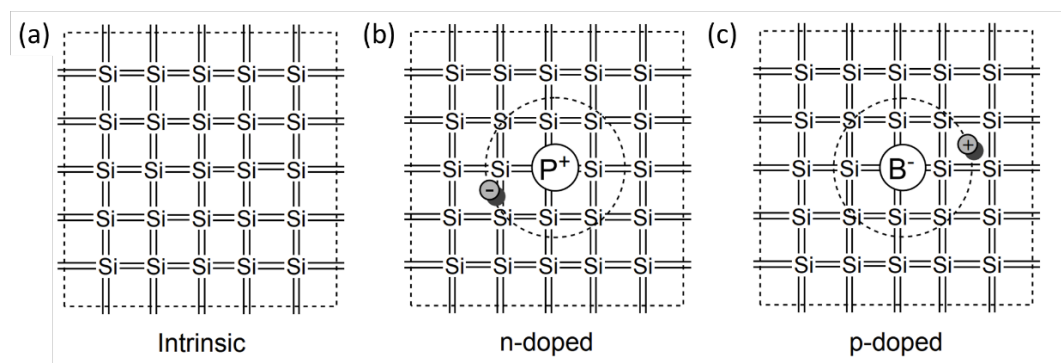
Figure 2.4. The examples of doping in Silicon [31].

2.4 Silicon heterojunction solar cells

SHJ solar cells represent a photovoltaic technology that leverages the unique properties of heterojunctions formed between c-Si and thin-film layers of a-Si or other materials [32]. The fundamental concept of a heterojunction involves the interface between two different semiconductor materials, each with distinct electronic properties. Thin layers of intrinsic and doped amorphous silicon are deposited on both sides of the c-Si wafer, forming heterojunctions. The (*i*)a-Si:H layers act as passivation layers, minimizing surface recombination of charge carriers (electrons and holes) and reducing losses in the solar cell. The heterojunctions at the interfaces between c-Si and doped a-Si layers create a built-in electric field due to the differences in electronic band structures. Photogenerated electron-hole pairs are efficiently separated and transported within the cell. The built-in electric field assists in the directional movement of charge carriers towards the respective electrodes, promoting efficient charge collection. The energy band alignment at the heterojunction interfaces is carefully engineered to facilitate charge separation and reduce recombination losses [33]. SHJ solar cells have demonstrated high conversion efficiencies, making them a promising technology for photovoltaic applications [7]. The reduced recombination losses, effective passivation, and optimized carrier transport contribute to the superior performance of SHJ solar cells [34].

2.5 Mechanism of loss and passivation

To achieve high-efficiency solar cells, a fundamental understanding of the sources and mechanisms of loss is essential. The losses in solar cells are generally categorized into two main types: optical loss and electrical loss.

2.5.1 Optical loss

Optical loss including reflection, parasitic absorption, and mismatch with solar

spectrum. Reflection take place in the front and rear surface of the cell. The application of anti-reflection coatings and surface texturing is used to reduce the reflection [35]. Parasitic absorption is an absorption process without the electron-hole pairs generation. Some sunlight is absorbed in non-active layers of the solar cell, such as the front contact, antireflection coating, or passivation layers [36].

2.5.2 Electrical loss

Recombination can be split into surface and bulk recombination [37]. Surface recombination is induced by surface defects. Dangling bond is a common type of surface defects which is produced by exterior Si atoms without a covalent band. The surface recombination rate R_s in n-type materials can be derived from Equation 2.1 and Equation 2.2

$$R_s \approx S_r\,(p_s - p_0) \qquad \text{Equation 2.1}$$

$$S_r = \vartheta_{th}\sigma_p N_{sT} \qquad \text{Equation 2.2}$$

where p_s is the concentration of minority charge carriers in n-type material and p_0 is the concentration of minority charge carriers in n-type material at equilibrium state. S_r is defined as the surface recombination velocity, v_{th} represents the thermal velocity in cm/s, σ_p is the capture cross-sectional area for holes, and N_{sT} is the surface trap density in cm^{-2}. The parameters v_{th}, σ_p, and N_{sT} are constants determined by the material properties and conditions at a specific temperature.

In the context of Equation 2.2 describing S_r, it is noteworthy that v_{th} and σ_p are constants, maintaining their values at a specific temperature within a solar cell. The variability of S_r is contingent upon changes in N_{sT}. Notably, the passivation layer applied to the semiconductor surface emerges as an effective strategy for diminishing surface recombination.

This understanding underscores the significance of managing the surface trap density through approaches like passivation techniques, aiming to optimize the performance of SHJ solar cells.

Bulk recombination in semiconductor materials encompasses three primary types: radiative recombination, Shockley-Read-Hall recombination, and Auger recombination as demonstrated in Figure 2.5.
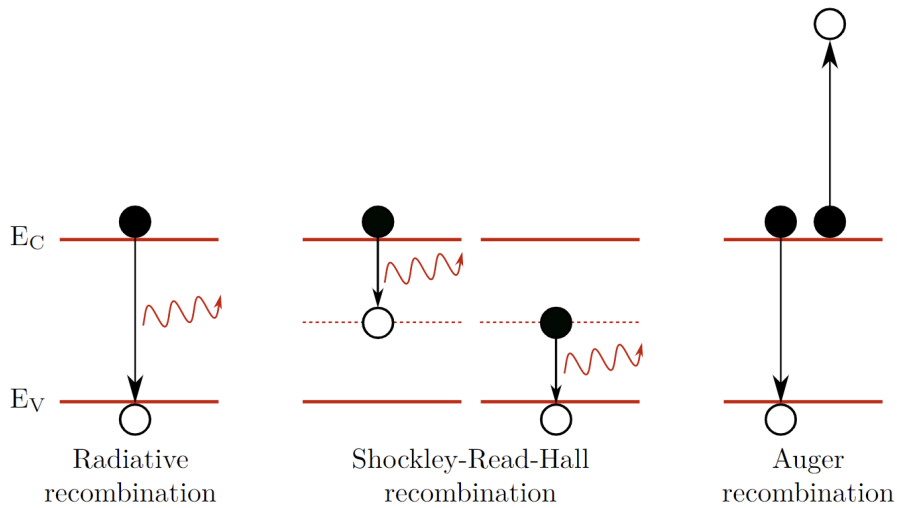
Figure 2.5 Basic mechanisms of recombination [38], [39]

Radiative recombination, also known as band-to-band recombination, does not play a dominant role in silicon solar cells. It operates inversely to the photon absorption process, involving the transition of charge carriers from the conduction band to the valence band, accompanied by the emission of a photon.

Shockley-Read-Hall (SRH) recombination takes place in the presence of defects or impurities within the band gap, earning it the alternative name of defect recombination. This recombination occurs in two distinct steps: an electron becomes trapped at a defect, subsequently recombining with a hole that is attracted to the trapped electron [40].

Auger recombination involves three particles in its process. The momentum and energy remaining from the recombination of electron-hole pairs are transferred to a third particle. This intricate process contributes to the overall recombination dynamics in semiconductor materials, impacting the performance of devices like solar cells. Understanding these mechanisms is crucial for enhancing the efficiency and functionality of such semiconductor-based technologies.

3. Equipment and Methods

3.1 Wafer preparation

3.1.1 Wafer parameters

The wafer is manufactured by the TOPSIL, which is a Danish company on the world market specializing in the production of ultrapure float zone silicon. There are two representative techniques that are used for growing monocrystal semiconductor. Cochralski (Cz) method is still the principal method for manufacturing monocrystalline silicon wafers. The Cz method have the advantages of equipment is relatively simple, process parameters are easy to be adjusted. But The monocrystalline Czochralski silicon (Cz-Si) wafer doping element longitudinal distribution is difficult to control. Another method is Float zone melting method (FZ), without the use of a melting crucible to prevent the crucible from introducing oxygen or metal impurities, and therefore can generate high purity single crystals. The TOPSIL FZ wafer used in this project to meet both the material requirements and the cost levels required in terms of high minority carrier lifetime, low levels of performance degrading impurities and tight resistivity tolerances. The parameters of n-type that doped with phosphorus TOPSIL wafer are shown in Table 3-1.

Table 3.1 The parameters of wafer used in this project

Diameter	Growth	Orientation	Resistivity	Thickness	Surface
99.6-100.2mm	Float zone (FZ)	<100>±1°	1-5Ω·cm	280±20um	polished

3.1.2 Wafer texture

The texture step is essential for enhancing light transmittance. In this project, the texturing process occurred in a solution with the rotation speed of the magneton set at 100 rpm. The solution consisted of 4 liters of deionized water (DI water), 1 liter of tetramethylammonium hydroxide (TMAH), and 120 mL of Alkatex 8. The temperature of the solution is maintained around 85-90°C. After thoroughly mixing the solution, the wafer was fully submerged below the water level for a duration of 15 minutes [41].

3.1.3 Wafer cleaning

The silicon wafer undergoes a thorough cleaning process. Initially, it is treated with a

60% HNO_3 for 10 minutes to remove external organic particles. Subsequently, it is rinsed with DI water for 6 minutes. To eliminate the surface oxide layer, a 3-minute treatment with hydrofluoric acid (HF) is conducted, followed by another 6-minute DI water rinse. The wafer is then spin-dried using a dryer.

For the standard cleaning procedure at the EKL lab, the wafer undergoes a triple cleaning cycle in the cleaning line. This line comprises two primary sections with HNO_3. The first section utilizes 99% HNO_3 at room temperature, followed by a DI water rinse. The second section involves treatment with 69.5% HNO_3 at 110°C, also followed by a DI water rinse. The wafer is immersed for 10 minutes in each HNO_3 bath, with corresponding DI water rinses of 5 minutes each.

Preceding PECVD process, the Marangoni system is employed for additional cleaning to eliminate the native oxide layer. The wafer is loaded into slots and subjected to a 5-minute etching process with 0.55% HF, followed by a final minute of treatment with isopropyl alcohol (IPA). The wafer is then rinsed in DI water for an additional 5 minutes.

3.2 Deposition techniques

Thin-film deposition techniques fall into three major categories: chemical vapor deposition (CVD), physical vapor deposition (PVD) and electroplating. In this section, a variety of deposition techniques for individual layers are described in detail.

3.2.1 CVD

Three widely employed CVD technologies in laboratory-scale research include low pressure chemical vapor deposition (LPCVD), plasma enhanced chemical vapor deposition (PECVD), and atomic layer deposition (ALD).

PECVD involves the deposition of thin layers on a substrate by leveraging glow discharge plasma to influence the process in conjunction with CVD. The thin film deposition technique, where plasma is typically generated using the radio-frequency method, is known as RF-PECVD. Amigo, an RF-PECVD cluster tool installed in the EKL Dimes lab, boasts six PECVD deposition chambers and a reliable transfer robotic manipulator, as depicted in Figure 3.1. This system is well-suited for depositing silicon-based intrinsic and doped thin film materials for various applications. In this project, the PECVD is applied to deposit $(i)/(n)/(p)$a-Si:H on the cleaned wafer as well as plasma treatment.
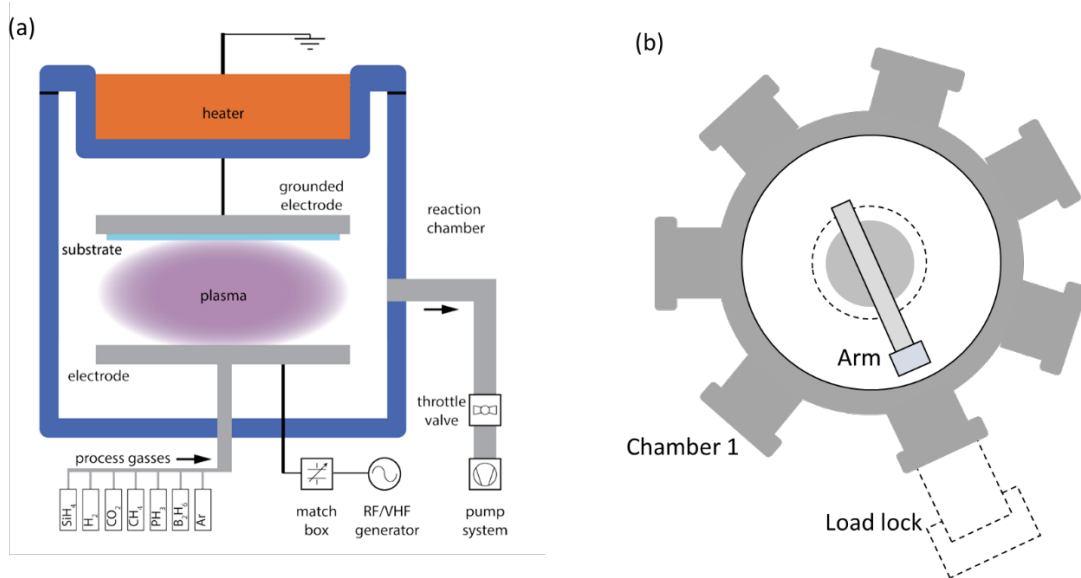
Figure 3.1 (a) Configuration of RF-PECVD setup and components [42], (b) Top view of Amigo

3.2.2 Evaporation

Compared with CVD, evaporation is a widely known PVD method for coating a thin film on the substrate in a vacuum environment. The two most frequently used evaporation ways are electron beam (e-beam) and thermal evaporation. The following Figure 3.2 shows an image of an E-beam and thermal evaporation equipment. Provac PRO500S is the evaporation facility that used in PVMD group and EKL lab, which is an organic whole of these two types of evaporation methods. In contrast to CVD), evaporation is a well-known method employed for coating thin films on substrates within a vacuum environment. The two most commonly used evaporation techniques are E-beam) and thermal evaporation. Figure 3.2 provides an illustration of E-beam and thermal evaporation equipment. The Provac PRO500S is the evaporation facility utilized in the PVMD group and EKL lab, encompassing both of these evaporation methods.

Figure 3.2 Sketch of (a) E-beam evaporation [43], (b) thermal evaporation [44]

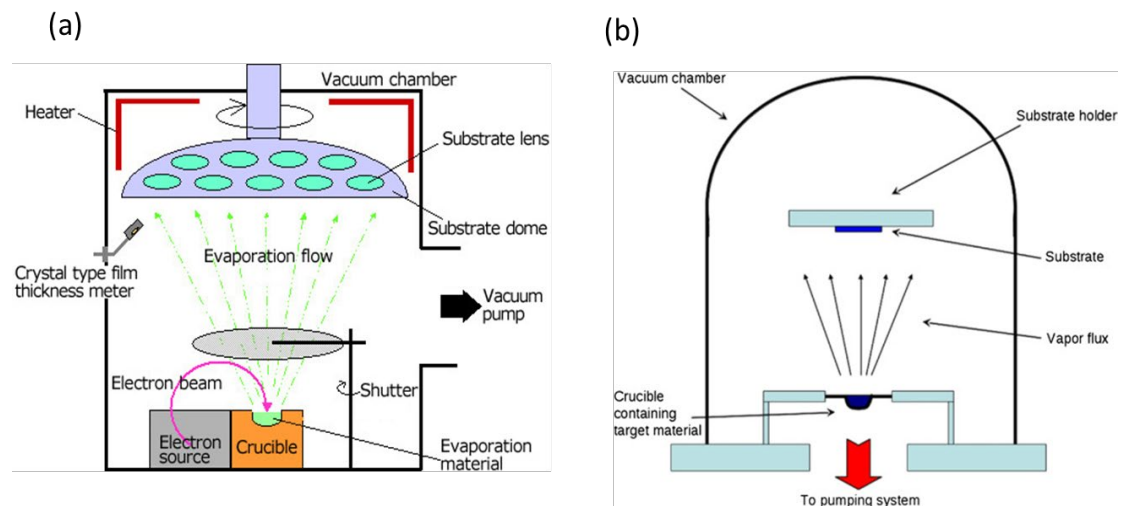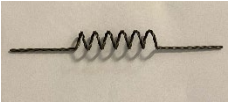E-beam evaporation, a form of PVD, comprises two main sections: an electron source and a crucible, as depicted in Figure 3.2 (a). The electron source generates and accelerates electrons into an electron beam, deflecting them as necessary. The crucible holds the material to be evaporated. For the deposition of the back contact metal aluminum (Al), E-beam evaporation technology is employed, achieving a 500nm deposition with a rate of 1nm/s.

Thermal evaporation, also known as resistive or resistive heating evaporation, is a straightforward technique that utilizes a resistance heating element or filament to heat a material in a crucible until it reaches its melting point. The vaporized material rises, and a thin layer is deposited on a substrate placed at the top of the chamber. The thermal evaporation process is illustrated in Figure 3.2 (b). Filament power supplies, requiring high currents of several hundred amps, ensure low-voltage safety. Accessory products such as "Boats", thin high-temperature metal sheets like tungsten with shaped indentations, are used for holding the material during evaporation.
In this project, dopant-free materials ($LiF/MgF_x/SrF_x/MoO_x$) and metals (Al, Ag) are deposited using thermal evaporation. The specific boats corresponding to different materials for thermal evaporation are listed in Table 3.2.

Table 3.2 The list of thermal evaporated materials

Material	Melting point (°C)	Pressure (mbar)	Deposition Rate (nm/s)	Boat
LiF	845	5E-6	0.03	
MgF_x	1261	5E-6	0.03	
SrF_x	1477	5E-6	0.03	
MoO_x	795	5E-6	0.1	
Al	660	5E-5	1	
Ag	962	5E-5	1	

In this project, CSC materials ($LiF/MgF_x/SrF_x/MoO_x$) and metal (Al, Ag) are deposited by thermal evaporation. Various boats corresponding to different materials' melting points for thermal evaporation are showing in Table 3.2.

3.2.3 Magnetron sputtering

Transparent conductive oxides (TCO) layers, primarily composed of oxides of In, play a crucial role as front/back contact electrodes and anti-reflection coatings in SHJ solar cells [45]. TCO layers offer numerous advantages, including improved trapping (reduced thickness and degradation) and low resistivity. In the realm of TCO, with examples like indium doped tin oxide (ITO) and indium tungsten oxide (IWO), indium doped tin oxide (ITO) stands out as a prominent choice. The ITO used in this work is composed of 90% indium oxide (In_2O_3) and 10% tin oxide (SnO_2). The IWO used in this work is composed of 95% indium oxide (In_2O_3) and 5% tungsten oxide (WO_3).

For the production of SHJ cells in this thesis, the ITO layer is deposited using the radio-frequency (RF) magnetron sputtering facility named Zorro. RF magnetron sputtering is a high-rate vacuum coating technique categorized under PVD. The fundamental mechanism is illustrated in Figure 3.3. In this process, the target or metal precursor to be deposited is bombarded with energetic ions from an inert gas (such as Argon or Helium). The powerful collision of these high-energy ions with the target releases target atoms into the vacuum. These metal atoms then deposit on the base material, forming a layer. Water is used to cool down the target and prevent excessive heating.
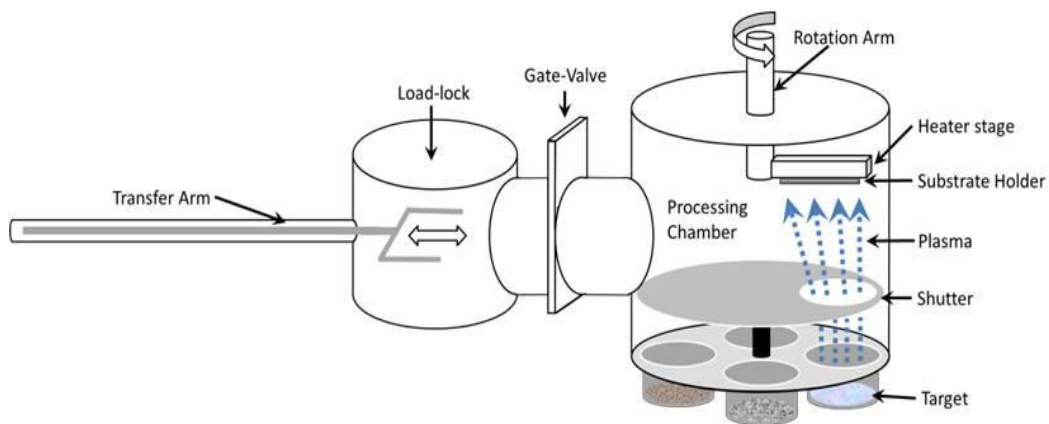
Figure 3.3 Sketch of RF magnetron sputtering system for TCO [46]

Leybold, another magnetron sputtering equipment, is used to deposit the rear-side metal contact for titanium (Ti) and silver (Ag) without breaking the vacuum, as shown in Figure 3.4. The supplier is Leybold Heraeus, and the PFG 2500 RF generator is applied to create an electric field between four different targets and the substrate. Ti and Ag are installed. The sputtering paprameters are listed in Table 3.3.

Figure 3.4 The outlook of magnetron sputtering equipment Leybold

Table 3.3 sputtering parameters in Leybold

Materials	Pressure (mbar)	Power (W)	Deposition rate (nm/s)
Ag	3.2E-6	250	8.8
Ti	3.2E-6	100	1.7

3.2.4 Screen printing

Screen printing (SP) is a mature, simple, and low-cost method used for front/back metallization in the manufacture of solar cells. It has been widely adopted in the commercial production of crystalline silicon solar cells due to its favorable characteristics. The process of screen printing is depicted in Figure 3.5.

Figure 3.5 Schematic representation of screen-printing process [47]

The silicon wafer is positioned between the screen and the bottom plate, and metal paste is applied. As the self-motion of printing initiates, pressure is applied to the squeegee, causing it to move at a specified speed across the screen. During this process, the paste is forced through the mesh onto the silicon wafer, leaving a grid pattern on the substrate.
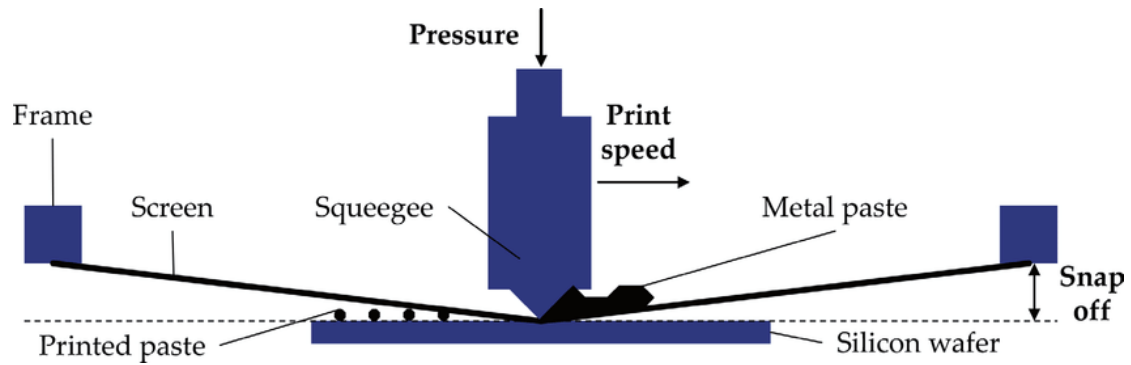
The metal paste used in this project is produced from DuPont. After completing the front pattern, it is crucial for SHJ solar cells to undergo a 30-second bake in a 170°C furnace. Subsequently, the back side screen printing is carried out. Following the formation of patterns on both sides, the SHJ cells must undergo baking at 170°C for 30 minutes, including an annealing process.

3.2.5 Photolithography

Photolithography, also known as optical lithography, is a technology employed for creating patterned features on a substrate. This process is particularly effective for achieving high precision printed patterns. Key components of the photolithography procedure include the light source, photoresist, and photomask. Typically, ultraviolet (UV) light serves as the light source, exposing the wafer through a patterned mask.

Photolithography follows a process outlined in Figure 3.6. Photoresist (PR) is a light-sensitive material applied to the surface of the prepared substrate using a spinner. Photoresists come in various types, with classification into positive and negative PR based on their chemical reaction mechanism and development principle. Positive photoresist becomes insoluble in the developer after exposure to light through the photomask. The chemical structure changes in a way that makes it resistant to dissolution when the substrate is immersed in the development solution. Before the PR spinning step, a seed layer of Ag with a thickness of 100nm, deposited by Leybold as mentioned in 3.2.3, is required.
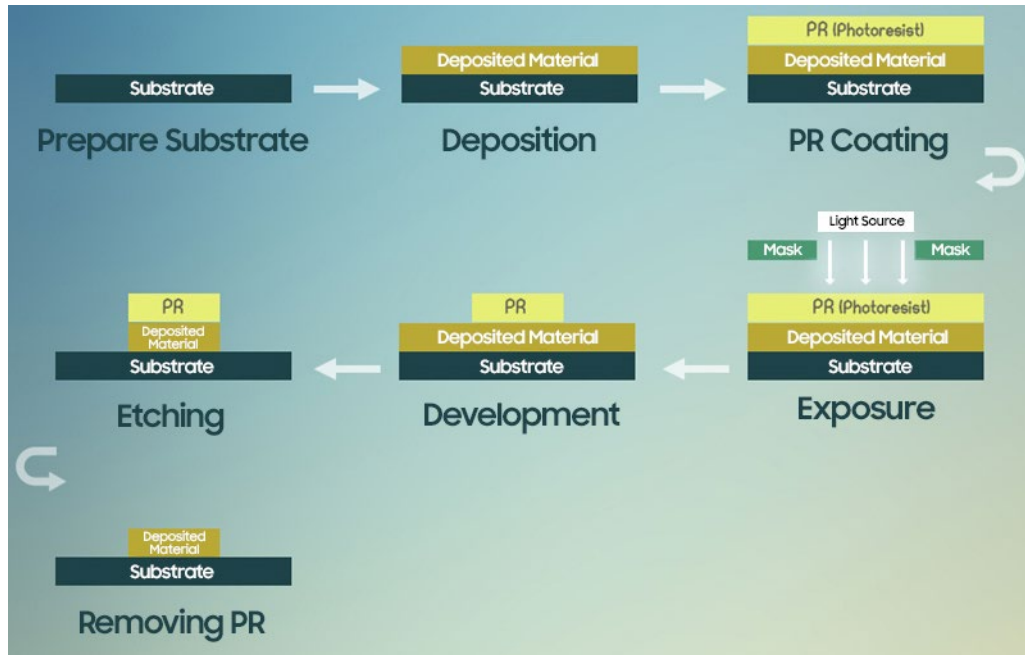
Figure 3.6 The flow chart of photolithography [48]

3.2.6 Copper plating

Seen from the operational principle, copper plating is another metallization method that deposits Cu metal on the surface of a solar cell, relying on the electrolytic method to collect charge carriers generated by PV effects. In comparison with screen printing, copper electroplating technology reduces the consumption of silver. This not only cuts down costs but also further improves the efficiency of solar cells. Figure 3.7 illustrates the setup of a copper plating cell, where copper functions as the anode, and a copper sulfate ($CuSO_4$) solution serves as a source of copper ions. When the wafer is completely submerged in the bath under a supply current, copper irons will migrate and appear on the region of wafer with a preexisting metal seed layer. In this case, we can realize copper plated fingers on SHJ solar cells.
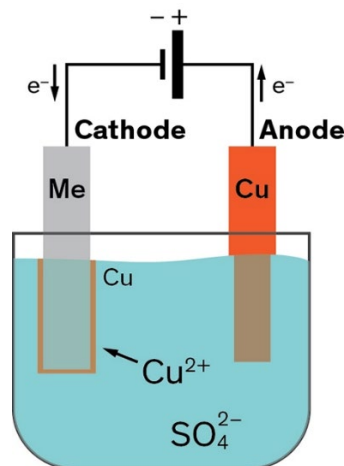
Figure 3.7 Image of electrolytic plating cell [49]

3.3 Characterization techniques

3.3.1 Spectroscopic Ellipsometry

Spectroscopic Ellipsometry (SE) is a characterization technique for PV thin-film material properties, offering contactless and non-destructive thickness measurement. With SE, sub-nanometer thickness can be measured rapidly in less than 1 second, allowing for the investigation of thin layer uniformity.

In our lab, the M-2000 Ellipsometer with auto-angle is employed to measure ultra-thin layer thickness and optical constants. The optical constants include two parameters, namely, refractive index (n) and extinction coefficient (k). n describes how light propagates through the medium, while k indicates the substance's ability to absorb light.

The M-2000 Ellipsometer comprises a light source, polarizer, analyzer, detector, and sample stage, as illustrated in Figure 3.8. This ellipsometer, developed by J.A. Woollam company [50], achieves a combination of high speed, accuracy, and precision. The accompanying software, CompleteEASE, is used with the M-2000 Ellipsometer for automated ellipsometry measurements.

Figure 3.8 M-2000 Ellipsometer with auto-angle front elevation [50], [51]

3.3.2 Reflectance and Transmittance

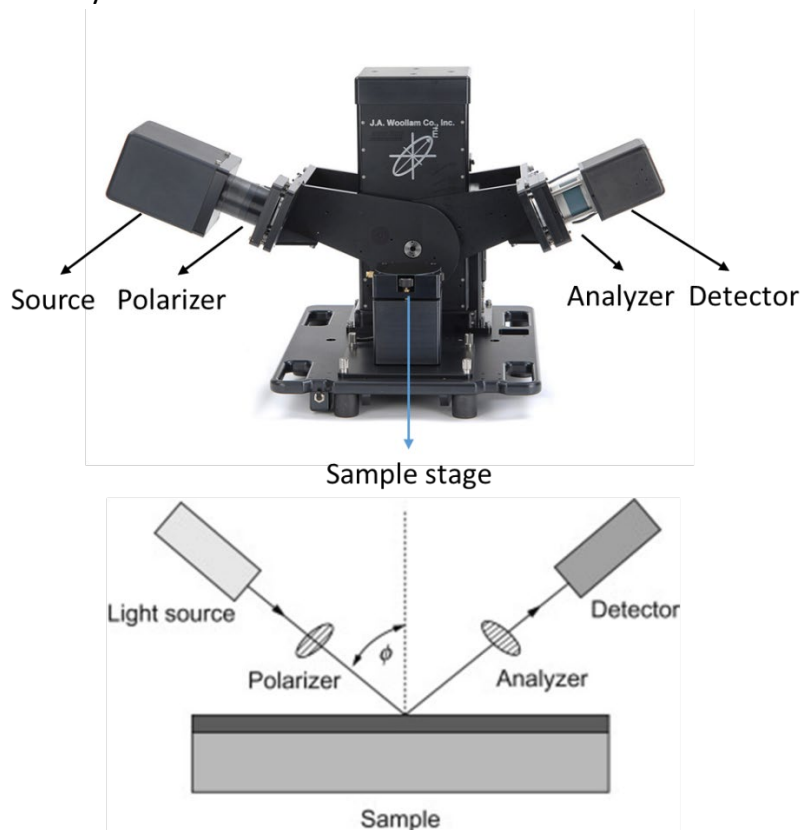The reflectance and transmittance are measured using the integrating sphere (IR) in conjunction with the PerkinElmer Lambda 1050+ UV/Vis/NIR Spectrophotometer. This spectrophotometer is specifically designed for the high-performance analysis of solar cells, featuring faster scan rates. A snap-in reflectance sphere with a diameter of 100mm is integrated into the spectrophotometer to capture both diffuse and specular reflectance [52].
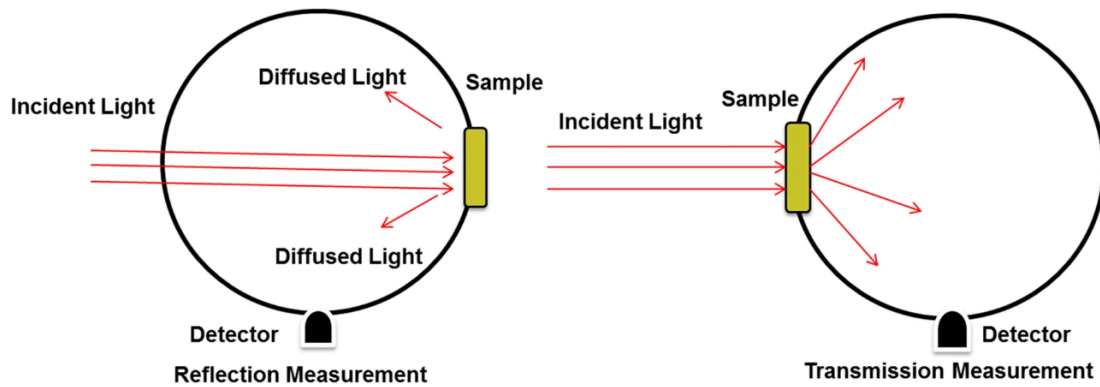
Figure 3.9 Total diffuse reflectance and transmission measurements by IR [53]

3.3.3 Minority Carrier Lifetime Tester

The minority carrier lifetime is contingent on the recombination rate, which is influenced by the concentration of minority carriers. Consequently, minority carrier lifetime serves as a crucial metric for evaluating solar cells.

The concentration of carriers maintains a dynamic equilibrium. When the number of minority carriers increases due to incident sunlight, the excess minority carriers undergo decay back to the equilibrium carrier concentration through the recombination process.

The recombination rate is intricately linked to the number of excess minority carriers. Two fundamental parameters integral to the recombination rate are minority carrier lifetime and diffusion length.

The minority carrier lifetime (τ_n or τ_p) of a material denotes the average time carriers can persist in an excited state before recombination occurs following electron-hole generation. Silicon wafers with longer lifetimes suggest that minority carriers generated in the bulk of the wafer by light will endure for an extended period before recombination. Solar cells crafted from wafers with higher minority carrier lifetimes are more likely to exhibit high efficiency compared to cells with shorter lifetimes. Therefore,

monitoring lifetime is paramount after each step in the solar cell manufacturing process.

In our lab, a Minority Carrier Lifetime Tester, specifically the Sinton WCT-120, is utilized for photoconductance measurement [20]. The diagram above Figure 3.10 given the introduction of Sinton WCT-120 minority carrier lifetime tester. Three parameters can be derived from the test result, which includes implied V_{oc} (i-V_{oc}), implied fill factor (i-FF) and lifetime (τ) etc.
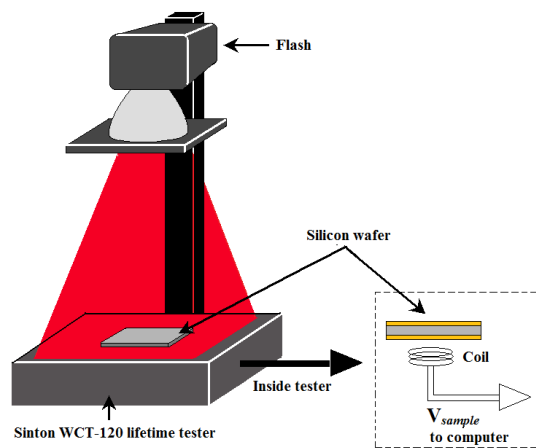
Figure 3.10 Sketch of minority carrier lifetime tester Sinton WCT-120 [54]

3.3.4 Contact resistivity

The transport properties of the electron contact stack are evaluated through the measurement of contact resistivity (ρ_c). The sample is applied to ρ_c measurements is different from the solar cell. The symmetric layer structure of contact resistivity sample involved in this project are drawn in Figure 3.11.
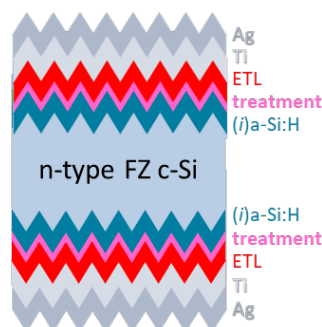
Figure 3.11 Sketchmatic structure of contact resistivity sample

3.3.5 Current-Voltage Measurements

The current-voltage measurement (*I-V* measurement) yields a characteristic *I-V* curve, providing detailed information and parameters about solar cell conversion efficiency and performance. These external parameters include open circuit voltage (V_{oc}), short circuit current density (J_{sc}), fill factor (*FF*), and peak power (P_{max}). The most critical parameter for evaluating solar cells is the conversion efficiency (η), which depends on the other parameters. The *J-V* curve follows the same principle. The *J-V* curve is obtained by continuously varying the bias voltage applied to a solar device under simulated sunlight irradiation and measuring current density. The line chart in Figure 3.12 provides a visualization of each parameter, explained in detail below.
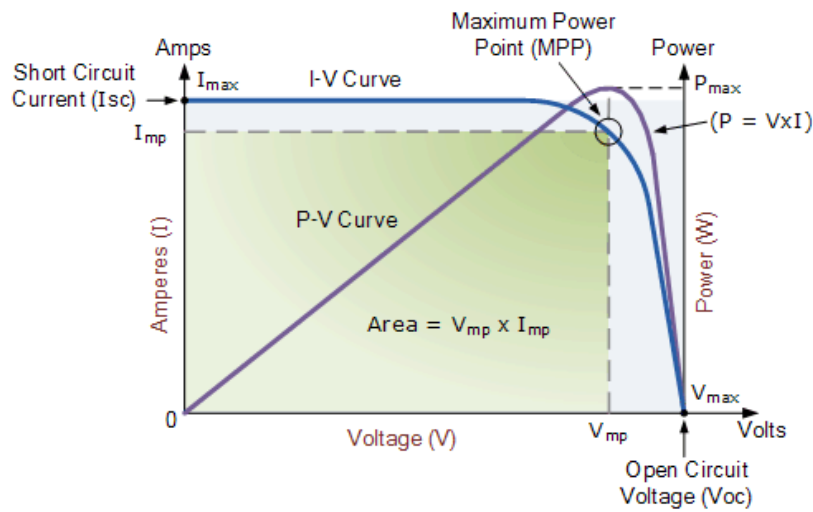
Figure 3.12 A typical *I-V* cure of a solar cell [55]

V_{oc} refers to the maximum voltage that can be measured in a solar cell at zero current. An equation for V_{oc} is given in Equation 3.1 [56],

$$V_{oc} = \frac{nkT}{q} \ln \left(\frac{I_{ph}}{I_0} + 1\right) \ \ or \ \ V_{oc} = \frac{nkT}{q} \ln \left(\frac{J_{ph}}{J_0} + 1\right) \qquad \text{Equation 3.1}$$

In which, J_{ph} is the photogenerated current density with small variation. J_0 is the saturation current density which is determined by recombination loss. Hence, recombination or saturation current density plays a major role in V_{oc}.

I_{sc} is the largest current drawn from a solar cell and located at the intersection point of the *I-V* curve and the vertical axis. I_{sc} is equal to photogenerated current (I_{ph}) in ideal condition. In order to facilitate the comparison of solar cells with different effective area, short circuit current density J_{sc} in mA/cm^2 took the place of I_{sc}.

FF can be represented by the ration of the green and blue areas in the Figure 3.12. The formula is as Equation 3.2,

$$FF = \frac{P_{max}}{P_{in}} = \frac{I_{mpp}V_{mpp}}{I_{sc}V_{oc}} = \frac{J_{mpp}V_{mpp}}{J_{sc}V_{oc}} \qquad \text{Equation 3.2}$$

η is calculated from the ratio of maximum power and incident power. At the standard test condition, I_{in} = 1000W/m^2, thus

$$\eta = \frac{P_{max}}{I_{in}} = \frac{J_{mpp}V_{mpp}}{I_{in}} = \frac{J_{sc}V_{oc}FF}{I_{in}} \qquad \text{Equation 3.3}$$

The Wacom solar simulator is capable of calculating the solar cell efficiency under 1-Sun illumination in standard test conditions (STC). The unified STC is developed to obtain reliable and comparable results, representing 1000 W/m^2 total irradiance on the solar cell with AM1.5 spectrum under constant 25°C conditions. The Wacom solar simulator uses two lamps (halogen and xenon) to create sunlight-resembling illumination.

3.3.6 External Quantum Efficiency

Quantum efficiency (QE) commonly referred as spectral responsivity (SR) or incident photon-electron conversion efficiency (IPCE) [57].

The relationship of QE and SR is illustrated by the following formula,

$$SR = \frac{q\lambda}{hc}QE \qquad \text{Equation 3.4}$$

Herein, q is the elementary charge (q = e = 1.60217634×10^{-19} coulombs [58]), h is Plank's constant (h = 6.626069×10^{-34} Js)

QE is an important parameter to characterize the photoelectric conversion ability of PV devices, which is used to describe the relationship between the number of photo-generated electrons and incident photons. The QE may be divided into two main categories. The internal quantum efficiency (IQE) can be defined as the fraction of charge carriers collected by the cell over the number of photons absorbed. The External Quantum Efficiency (EQE) is the ratio of the number electron-hole pairs collected in the solar cell to the number of photons from the light source. The EQE is then determined as

$$EQE(\lambda) = \frac{I_{ph}(\lambda)}{q\Psi_{ph,\lambda}} \qquad \text{Equation 3.5}$$

Where I_{ph} is photogenerated current, and $\psi_{ph,\lambda}$ is the spectral photon flow incident on the solar cell. The values of EQE are a result of a multiple factors, including optical loss (parasitic absorption) and electrical loss (recombination losses).
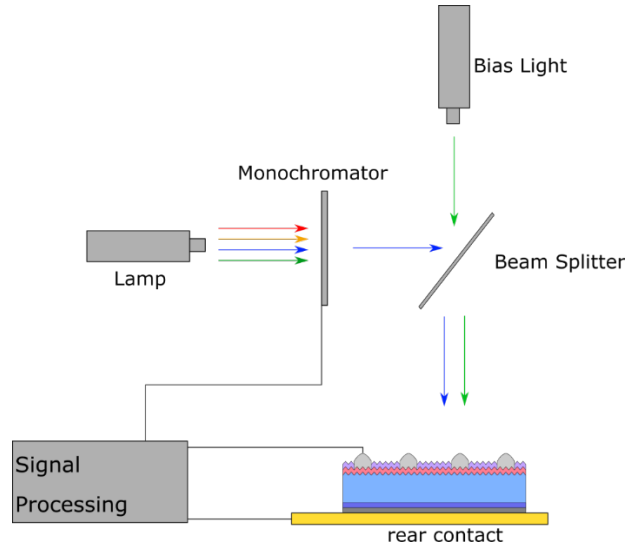
Figure 3.13 Working diagram of EQE

The measurement theory diagram of EQE is shown in the Figure 3.13. When measuring EQE, the calibrated photodetector with known EQE is used from 300 to 1200nm. By means of photodetector, the spectral photon flow incident could be got as

$$\Psi_{ph,\lambda} = \frac{I_{ph}^{ref}(\lambda)}{qEQE^{ref}(\lambda)}$$
 Equation 3.6

Then, the $EQE(\lambda)$ is derived as

$$EQE(\lambda) = EQE^{ref}(\lambda)\frac{I_{ph}(\lambda)}{I_{ph}^{ref}(\lambda)}$$
 Equation 3.7

That means the measurement of EQE could be carried out from two current measurements by Ampere meter.

Another parameter value is also computed as

$$J_{sc} = -q\int_{\lambda_2}^{\lambda_1} EQE(\lambda) \; \Phi_{ph,\lambda}^{AM1.5}d\lambda$$
 Equation 3.8

With the spectral photon flux $\phi_{ph,\lambda}$

3.3.7 Suns-V_{oc}

In Suns-V_{oc} measurement, the probes are directly contact with the busbar at the front of solar cells and metallization layer. As the result, the illumination-V_{oc} curve can be measured out. The Suns-V_{oc} MX stage from Sinton (product drawing as shown in Figure 3.14) is established in ESP lab.

Figure 3.14 The Suns-V_{oc} MX stage from Sinton [59]

The parameters reported for Suns-V_{oc} measurements comprise pseudo-efficiency (*pEff.*) and Pseudo-fill-factor (*pFF*). The difference between *pFF* and *FF* reflects the electrical loss.

4. Integration of dopant-free materials as electron transport layer in SHJ solar cells

4.1 Raw materials

Lithium fluoride (LiF), an alkali halide characterized by a wide band gap of 13.6eV [60], stands as an inorganic compound renowned for its utility in optical and electronic devices. Its distinguished attributes include commendable conductivity, a high refractive index, and superior transmittance [61]. Meanwhile, magnesium fluoride (MgF_x), boasting a substantial band gap of 10.8eV and a refractive index of 1.38 at 550nm [62], shares a similar prowess in optical applications. Similarly, strontium fluoride, possessing a wide band gap of 9.73eV [63], showcases exceptional optical characteristics, including a low refractive index and heightened transmission within the infrared and ultraviolet spectral ranges.

The detailed specifications of these three metal fluorides are summarized in Table 4.1. These materials, characterized by their wide band gaps, exhibit promising potential in manufacturing non-toxic and dopant-free electron transport layers for SHJ cells. The thermal evaporation process for all metal fluorides occurred under a pressure of 5×10^{-6} mbar, with a rotation rate of 10rmp. Achieving a uniformly distributed electron transport layer necessitated a deliberately slow deposition rate of 0.03 nm/s.

Table 4.1 Provenance and purity of materials used in this study

Material	Supplier	Metallic purity	Melting point [°C]
LiF	Sigma-Aldrich	99.995%	845
MgF_x	Umicore	99.99%	1261
SrF_x	Sigma-Aldrich	99.9%	>1400 [64]

4.2 Fabrication

Figure 4.1 is the flow chart of cell fabrication. Each fabrication step is discussed in a specific chapter as illustrated in the flow chart.
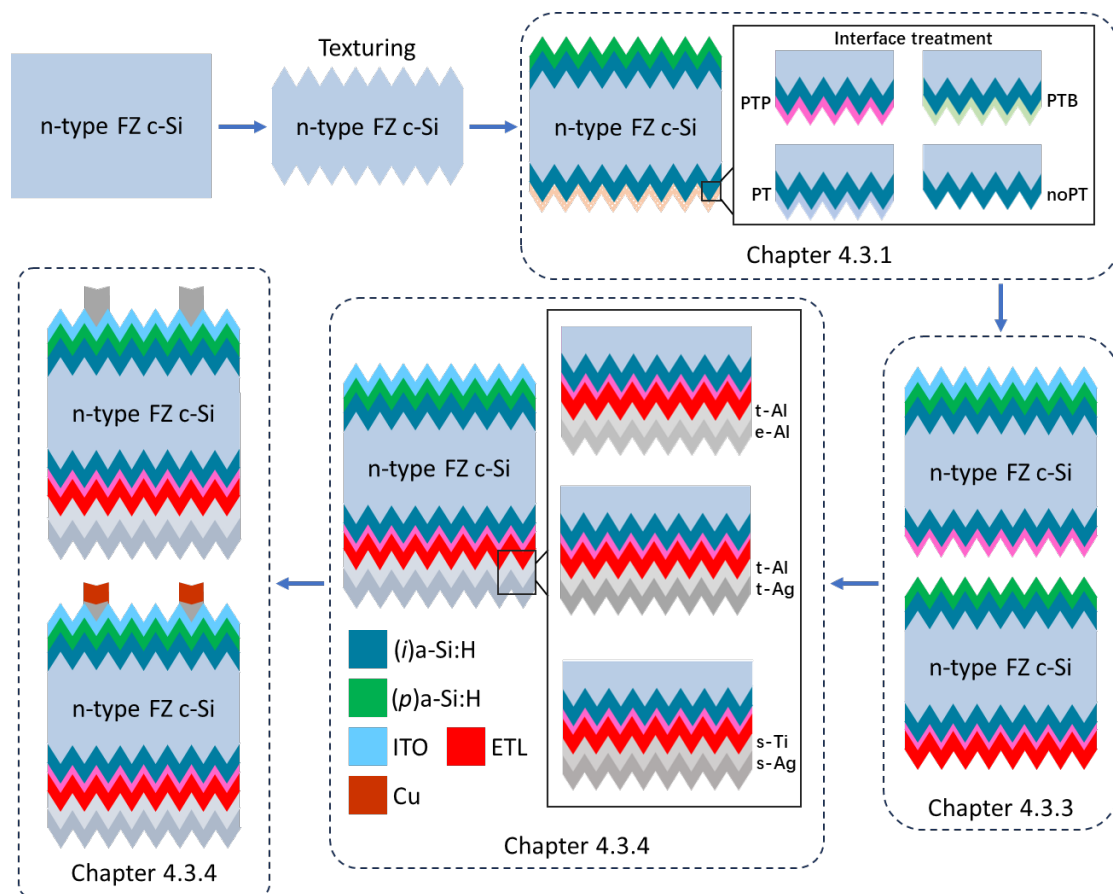
Figure 4.1 Flow chart of cell fabrication

4.3 Optimization of LiF-based dopant-free SHJ solar cells

4.3.1 Plasma treatments

Why plasma treatment?

Different treatments at the (*i*)a-Si:H/LiF interface are investigated to understand the effects of plasma treatments on LiF properties. Four distinct scenarios are explored subsequent to the deposition of identical (*i*)a-Si:H on the cell.

The primary focus is to evaluate the influence of interface treatments on cell performance. Specifically, a consistent 1nm LiF layer is maintained on the rear side while varying interface treatments are applied to the LiF/(*i*)a-Si:H interface. The lifetime of cell precursors is quantified using Sinton measurements after PECVD. The measured lifetime, represented in Figure 4.2, serves as an indicator for assessing the passivation quality of the precursors, as detailed discussed in Section 3.3.3.

Figure 4.2 illustrates the lifetime variations among different treatments. The PTP samples exhibit a fluctuating lifetime range spanning from 8ms to 14ms, with the highest

recorded value reaching 14ms, representing the best passivation among these inter-
face treatments. Conversely, the noPT samples demonstrate a slightly lower lifetime in
comparison to the PTP samples. Notably, the highest lifetime achieved by the PT sam-
ples at the same level compared with noPT treatments. This suggests that PT treat-
ments have the potential to achieve a passivation quality as noPT samples. However,
the PTB samples exhibit the lowest recorded lifetime among all treatments. The differ-
ence can be attributed to the presence of borane gas during the treatment process.
According to prior research, the inclusion of borane gas has negative effect for the
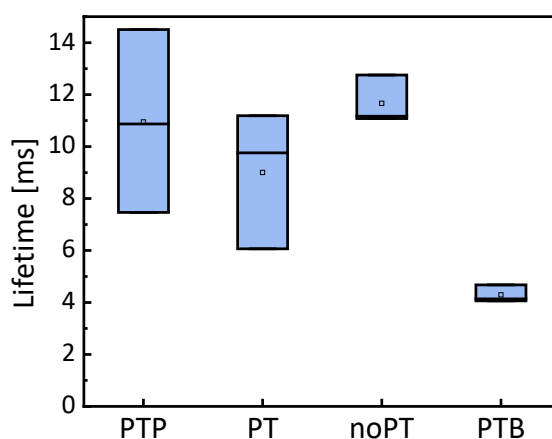passivation quality of (i)a-Si:H [20].

Figure 4.2 Lifetime of precursors after different interface treatment

Subsequently, we fabricated solar cells with the cell precursors. The extracted data of
J-V measurement data as shown in Figure 4.3, encompassing plots for PTP, PT, and
noPT samples. Notably, the J-V curve for PTB samples demonstrates an S-shaped prop-
erty, characterized by a lower FF, likely due to the introduction of a thin p-type layer
during PTB treatment. Analysis of the J-V curves reveals distinct trends among treat-
ments. Cells treated with PTP exhibit the highest V_{oc} values, while both PT and noPT
samples show comparable V_{oc} levels. This observed V_{oc} trend aligns closely with the
lifetimes of the cell precursors. It emphasizes the relationship between surface pas-
sivation and V_{oc}, with PTP treated cells showing superior surface passivation compared
to PT and noPT treatments. Moreover, the J_{sc} values further highlight treatment differ-
ences. PTP samples demonstrate higher J_{sc} values than PT and noPT samples, at-
tributed to the higher EQE observed beyond 800nm, as depicted in Figure 4.4. The
introduction of a specific layer on the rear side might influence the response to longer
wavelengths, contributing to the increased J_{sc} observed in PTP-treated cells.

The FF across these treatments remains relatively similar. Consequently, the efficiency
of solar cells is predominantly influenced by V_{oc} and J_{sc}, resulting in higher efficiency in
PTP treated cells among all treatments. Given the superior performance of PTP treat-
ment, subsequent investigations studied on the impact of thickness variation on cell
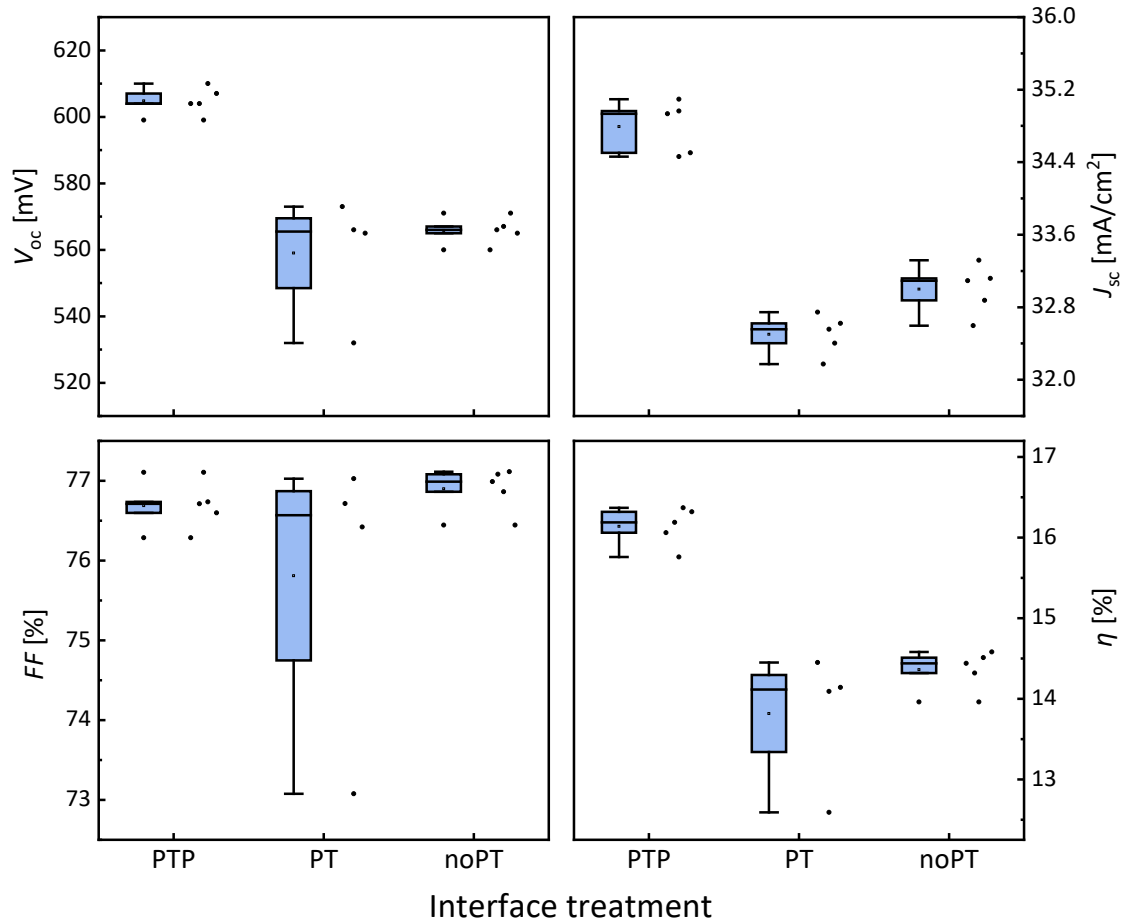performance.

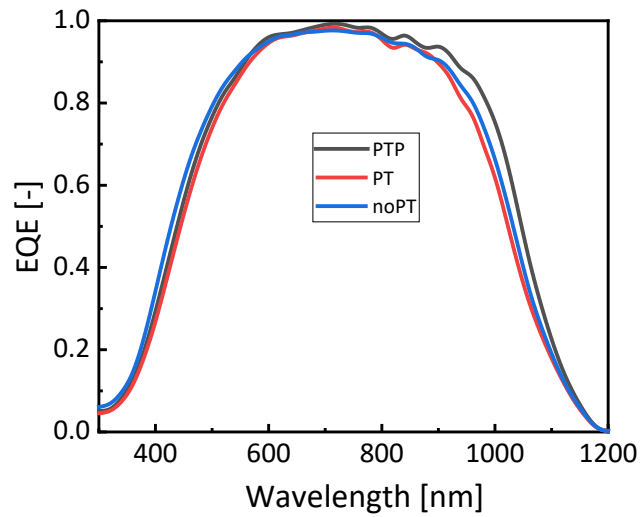Figure 4.3 External parameters of SHJ solar cells with different interface treatments

Figure 4.4 EQE of SHJ solar cells with different interface treatments

4.3.2 Optimal thickness

With the experiment from last section, we found that the optimal interface treatment

is PTP. We proceeded to deposit varying thicknesses of LiF, ranging from 0 to 5nm. 0nm-LiF means the reference cell. The data extracted from this study is illustrated in Figure 4.5.
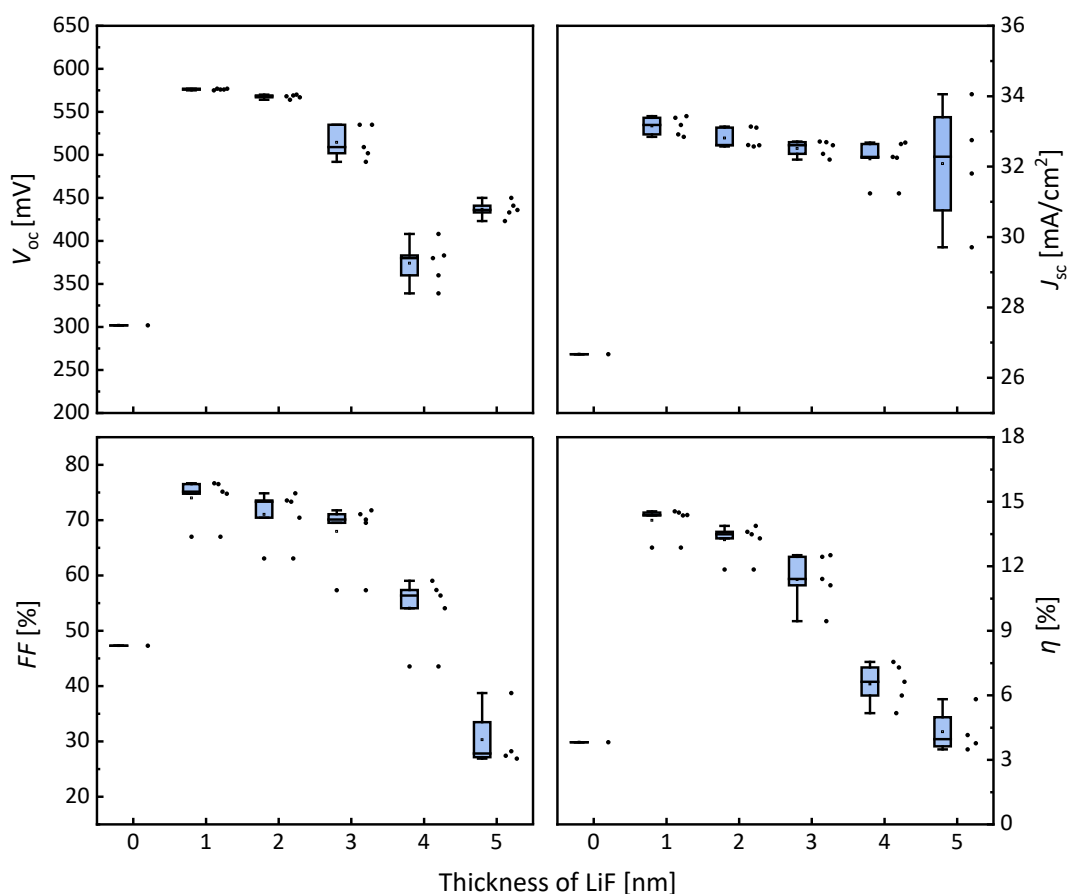

Figure 4.5 External parameters of SHJ solar cells with different thickness of LiF. In the range of 1 to 4 nm, all four parameters of LiF exhibit values higher than those of the reference cell. Additionally, the *J-V* curve of both the reference sample and the 5nm-LiF display an S-shape. Upon varying LiF thickness, we observed a consistent trend: the V_{oc} of cells generally decreases as the LiF thickness increases, with one exception observed at 5nm, where there is a slight increase from 400mV to 450mV. However, the overall lower V_{oc} levels could potentially be attributed to screen printing techniques.

Correspondingly, the J_{sc} decreases with the increasing thickness of LiF. Although LiF is transparent within the visual light range, thicker LiF layers tend to induce higher parasitic absorption within the LiF layer itself. This absorption negatively impacts the J_{sc}. It is clear that both the *FF* and J_{sc} exhibit a similar decreasing trend. This phenomenon is linked to the introduction of higher contact resistivity associated with thicker LiF layers, as explained in prior research [13]. An interesting thing within the J_{sc} of 5nm samples performed fluctuation. This behavior might be correlated with the S-shaped *J-V* curve observed in these samples. Specifically, when a device displays an S-shaped *J-V* curve, the J_{sc} exhibits fluctuations, as illustrated in Figure 4.6 [65].

The trend in *FF* is obvious. For 1nm thick sample, *FF* peaks at 76.65% but sharply declines to 19.74% with increased LiF thickness. Efficiency serves as a comprehensive measure of solar cell performance, heavily influenced by *FF* and J_{sc}. Considering efficiency, the data strongly suggests that a 1nm LiF thickness is optimal. The investigation of contact resistivity within the LiF/Al interface on an *n*-type wafer reveals a notable correlation with the choice of alkali metal fluoride, as detailed in James Bullock's comprehensive study [66]. Within the nanoscale thickness range of 0.5-1.5nm, the LiF/Al stuck producing the lowest contact resistivity values. However, the ρ_c value exhibited a progressive increment with increasing thickness of the LiF layer. 1nm thickness aligns with higher *FF*, emphasizing its crucial role alongside J_{sc} in determining overall cell performance.
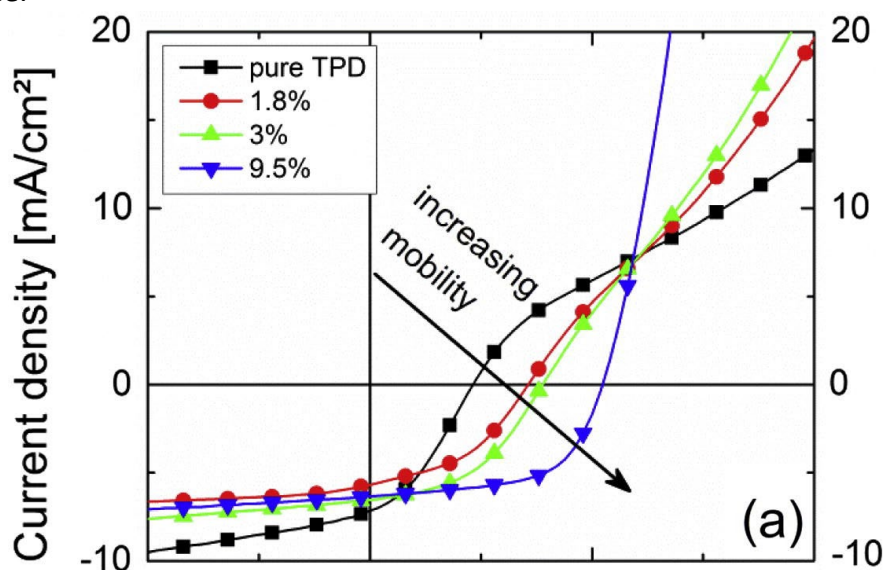

Figure 4.6 Standard *J-V* curve and S-shape *J-V* curve [65]

4.3.3 LiF-ITO deposition order

After optimizing the LiF thickness, our interest turned to investigating the influence of the deposition sequence involving ITO and LiF. The ITO deposition process, involving sputtering, might induce ion bombardment, impacting the surface condition of the rear side [67]. In this experimental, we utilized a 1nm LiF layer combined with PTP as the interface treatment. The extracted cell data is depicted in Figure 4.7, where the x-axis labels indicate the deposition sequence of ITO and LiF following PECVD.

Specifically, "ITO-LiF" denotes ITO deposition on the plasma-treated sample followed by LiF, while "LiF-ITO" represents the reverse deposition order. The LiF-ITO samples exhibit higher V_{oc}, J_{sc}, and *FF*, consequently resulting in superior efficiency. We considered that this enhancement is attributable to the protective role of LiF over (*i*)a-Si:H, ensuring its properties during the deposition process involving ITO.
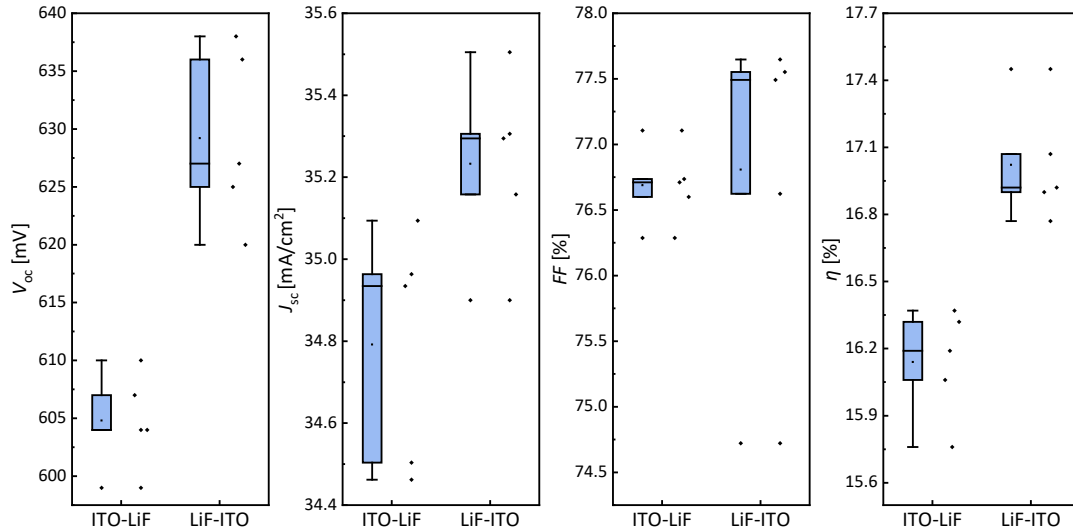
Figure 4.7 External parameters of SHJ solar cells with different deposition order of LiF and ITO

4.3.4 Metallization

The choice of metal contact significantly impacts the electronic performance of solar cells. We evaluated three rear side metallization contact combinations and visualized their external parameters in Figure 4.8. Our approach involved employing two metal layers for rear side contact. The x-axis in Figure 4.8 illustrates the upper metal deposition order, where "t-Al" signifies thermally evaporated Al and "e-Al" represents e-beam evaporated Al, with respective thicknesses of 10nm and 500nm. Additionally, "t-Ag" refers to thermally evaporated silver at a thickness of 500nm, while "s-Ti" and "s-Ag" denote sputtering-evaporated 10nm-thick Ti and 500nm-thick Ag, respectively.

Initially, we adopted a metal contact resembling the structure of the virgin cell, utilizing thermal evaporated Al in conjunction with e-beam deposited Al. The choice of Al aimed to minimize the working function mismatch between LiF and Al [68]. The t-Al was gently deposited first, potentially serving as a buffer layer to protect passivation effects from ion bombardment. Subsequently, considering replacing the aggressive e-beam Al [69], we explored thermal evaporated Ag. However, this process introduced a potential drawback, where t-Al and t-Ag necessitated vacuum breaking, potentially leading to the formation of a thin AlO_x layer between them. As an alternative, we explored sputtering-evaporated Ti and Ag, completed in a single vacuum condition.

The external parameters, extracted from *J-V* measurements, are displayed in Figure 4.8. The samples utilizing e-Al exhibited lower V_{oc} compared to the other two metal contacts. However, the J_{sc} value of e-Al samples exceed other metal contacts, likely attributable to the lower *FF* observed in this sample set. Lower *FF* samples consistently exhibited unusually higher J_{sc} values. Meanwhile, the J_{sc} and *FF* values for t-Al/t-Ag and

s-Ti/s-Ag samples appeared comparable, indicating that efficiency was primarily influenced by the V_{oc} trend in these cases.
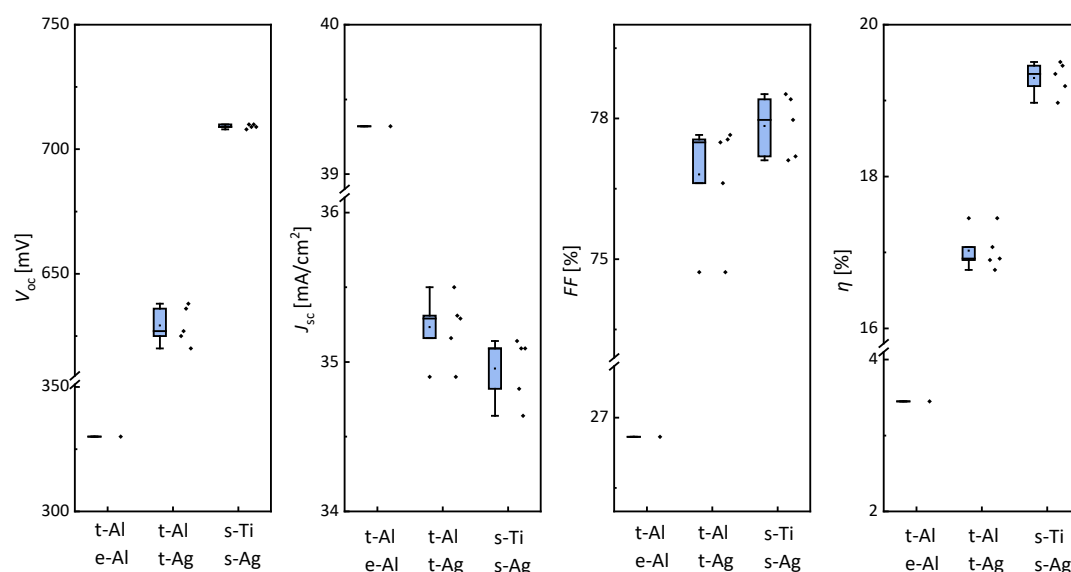

Figure 4.8 External parameters of SHJ solar cells with different back metal contact

Next, we turned our attention to the metallization process on the front side of the solar cells. Specifically, we conducted a comparative analysis between samples utilizing screen printing (SP) and copper plating (CP) as metallization methods, the results of which are depicted in Figure 4.9.

The observed V_{oc} differences between SP and CP samples can be attributed to the varying passivation quality of the cell precursors. Notably, CP samples demonstrated higher J_{sc} values, attributable to their well-controlled grid width, which was thinner compared to SP samples. Copper-plated electrodes exhibit a significantly lower resistivity, approximately 2–3 times less than printed silver electrodes, owing to their absence of voids in the structure [70]. Moreover, the width of Cu plate electrodes can be reduced, much finer compared to the screen-printed Ag grids, thereby notably decreasing grid shading [71].

Interestingly, while SP and CP samples exhibited similar average FF, CP samples show a capacity to achieve a higher FF, nearing 80%. As a consequence, the CP samples displayed higher efficiency compared to SP samples, emphasizing the significance of the metallization process in influencing overall solar cell performance.
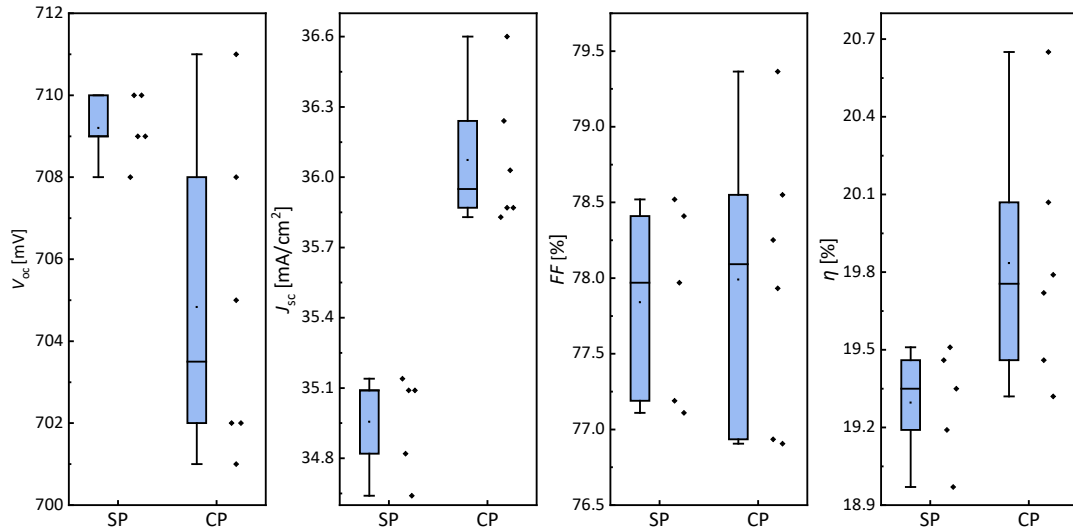
Figure 4.9 External parameters of SHJ solar cells with different front side metal

Based on our prior investigations, several crucial conclusions can be drawn. Firstly, PTP emerges as the optimal interface treatment for enhancing solar cell performance. Moreover, our studies indicate that a 1nm thickness of LiF yields optimal cell efficiency. Investigating the sequence of ITO and LiF deposition revealed superior cell performance when LiF was deposited first.

Furthermore, our exploration into rear side metal contact stacks exposed that sputtered Ti/Ag combinations exhibited the best compatibility with LiF. On the front side, employing copper plated fingers significantly improved overall efficiency.

In light of these discoveries, our future investigations will expand upon our findings based on LiF, extending the study to encompass MgF_x and SrF_x materials. This expansion aims to explore potential similarities and capitalize on the insights gained from our research on LiF to further enhance solar cell performance.

4.4 Exploration of MgF_X and SrF_X as ETL materials

4.4.1 MgF_x as ETL material

The optimal parameters are applied in MgF_x SHJ solar cells to study the thickness influence on device performance. The external parameters as shown in Figure 4.10. The four parameters of MgF_x, ranging from 1 to 5 nm, consistently exhibit higher values compared to those of the reference cell. The V_{oc} demonstrated a gradual rise from 1 to 3nm, achieving a peak over 710mV. Subsequently, the 4nm MgF_x layer maintained a consistent V_{oc} within the range of 690-710mV, same as 3nm layer. Interestingly, the 5nm MgF_x layer exhibited the highest V_{oc} among these layers, even with a marginal

increase compared to the 3nm layer. This enhancement is potentially attributed to the effective passivation coming from the thicker MgF_x layer.

In terms of J_{sc}, the curve depicted fluctuations within the range of 35.6 to 37.0 mA/cm^2. Simultaneously, the EQE measurement results illustrated in Figure 4.11 revealed significant insights. The 3nm samples exhibited a relatively lower and narrower curve in comparison to other samples, potentially due to issues encountered during the fabrication process. Additionally, the conspicuous high point observed in the 2nm samples correlates with lower *FF* values, a characteristic often associated with S-shaped *J-V* curves in this context [65].

The *FF* of the 1nm MgF_x layer showcased its peak, nearing 80%. In contrast, the *FF* demonstrated a decrease with the increasing thickness for 2-4nm MgF_x layers, as observed [72] [73]. The *FF* of 2nm cells exhibited considerable dispersion, ranging from 57% to 75%. Additionally, a small increment in *FF* for the 5nm MgF_x layer is obvious from Figure 4.10, indicating the potential for further investigation into the performance of the 5nm MgF_x layer.

Yimiao conducted a study investigating the relationship between contact resistivity and the thickness of MgF_x. The research revealed that the minimum ρ_c value, standing at approximately 35 mΩ·cm^2, occurred at a thickness of 1nm for MgF_x [74]. This consistency reinforces the validity and significance of our research. Moreover, the efficiency and *FF* displayed same trends across various thicknesses of MgF_x. Considering the combined influence of high *FF* and efficiency, the optimal thickness appears to be the 1nm MgF_x layer.
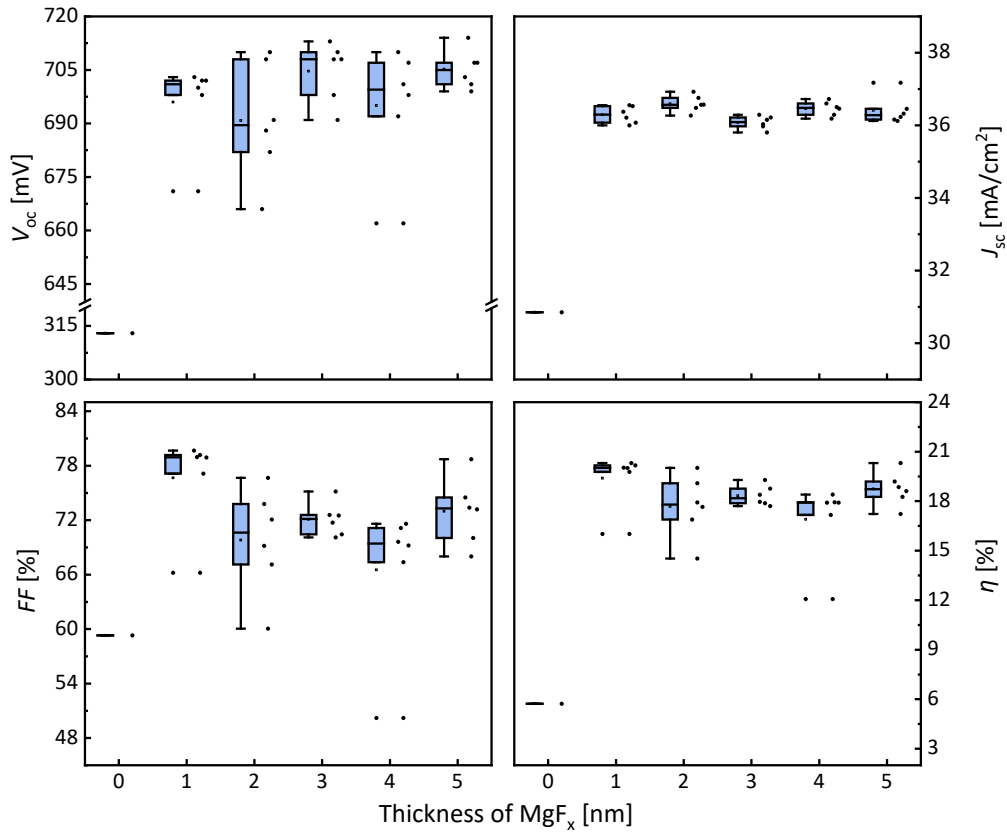
Figure 4.10 External parameters of SHJ solar cells with different thickness of MgF$_x$

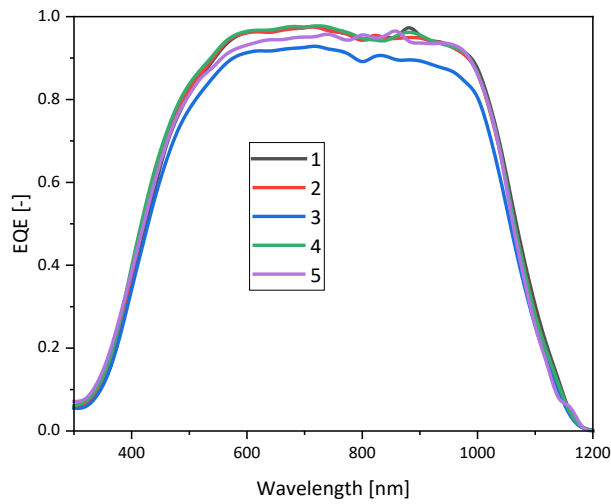

Figure 4.11 EQE of SHJ solar cells with different MgF$_x$ thickness

4.4.2 SrF$_x$ as ETL material

The optimal parameters are implemented in SrF$_x$ SHJ solar cells to investigate how thickness influences device performance, utilizing the external parameters illustrated

in Figure 4.12. The V_{oc} remains consistently high, around 710mV, for the 1-4nm SrF$_x$ layers. However, the V_{oc} of the 5nm samples exhibited fluctuations, possibly stemming from variations in the layer deposition process. Non-uniformity in layer deposition might have resulted in differing passivation quality across different areas of the wafer. In terms of J_{sc}, the performance showcased a reverse V-shape trend, peaking at the highest value with the 3nm layer.

Regarding *FF*, a slight increase is observed from 1nm to 2nm, followed by a decline at 3nm. However, the highest *FF* value is achieved at 4nm, decreasing again at 5nm. While drawing definitive conclusions proves challenging, observations align with previous research [75], [76], indicating that the optimal thickness might be 4nm. The overall trend suggests that SrF$_x$ exhibits characteristics of thickness tolerance, implying that the performance of SrF$_x$ -based SHJ solar cells is relatively insensitive to changes in SrF$_x$ thickness [77].

Furthermore, a slightly increase in efficiency at 4nm compared to other thicknesses leads us to conclude that the optimal thickness for SrF$_x$ might indeed be 4nm. This alignment with previous findings, coupled with the efficiency trend, suggests the potential superiority of the 4nm thickness in enhancing overall cell performance.
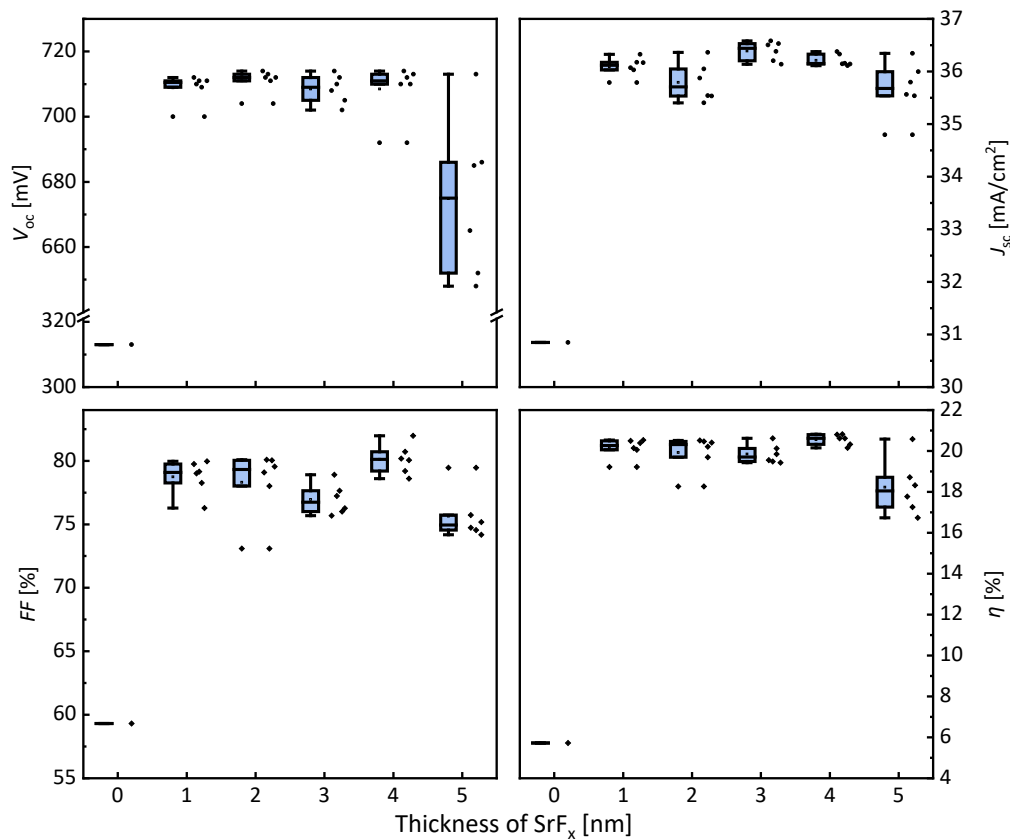

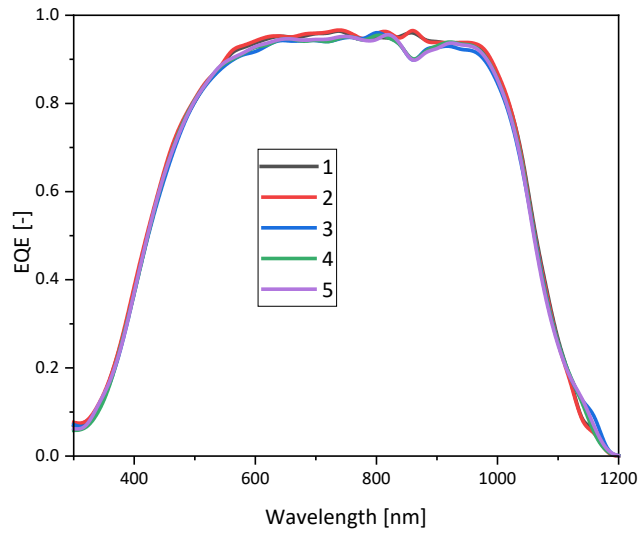Figure 4.12 External parameters of SHJ solar cells with different thickness of SrF$_x$

Figure 4.13 EQE of SHJ solar cells with different SrF$_x$ thickness

5. Application of dopant-free materials on front/back of SHJ solar cells

The primary objective of this study is to fabricate SHJ solar cells incorporating dopant-free HTL and ETL on both the front and rear sides. Building upon our prior research, we have amalgamated the optimal parameters identified for LiF, MgF_x, and SrF_x. On the front side, we have utilized MoO_x as the HTL, following the baseline from the PVMD group, with PTB applied during the deposition of MoO_x [20]. The optimal thickness applied in the cells as shown in Table 5.1. The cell structure is depicted in Figure 5.1.

On the rear side, PTP is applied during the deposition of LiF, MgF_x, and SrF_x, with the specific parameters outlined in the provided table. The extracted external parameters are presented in Figure 5.3, with each box containing data from 12 cells. For this phase of the work, we have selected comparable cell precursors with similar levels of lifetime. Notably, in terms of V_{oc}, MgF_x yields the highest value, followed by SrF_x and LiF.

The light response of these cells demonstrates similarity, achieving approximately 38 mA/cm^2 in J_{sc}. This J_{sc} result correlates with the EQE findings as shown in Figure 5.2. LiF and MgF_x cells can attain FF above 74%, whereas SrF_x only reaches 72%. In conclusion, MgF_x provides the highest efficiency, followed by LiF and SrF_x.

Table 5.1 Thickness of HTL and ETL

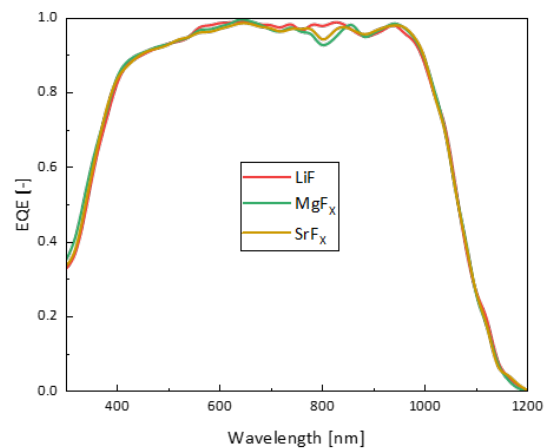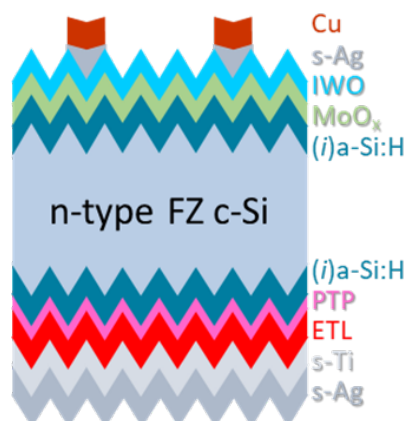| Material	Function	Thickness (nm)
MoO_x	HTL	1.7
LiF	ETL	1
MgF_x	ETL	1
SrF_x	ETL	4

Figure 5.1 The cell structure of dopant-free SHJ solar cell   Figure 5.2 EQE of dopant-free SHJ solar cell
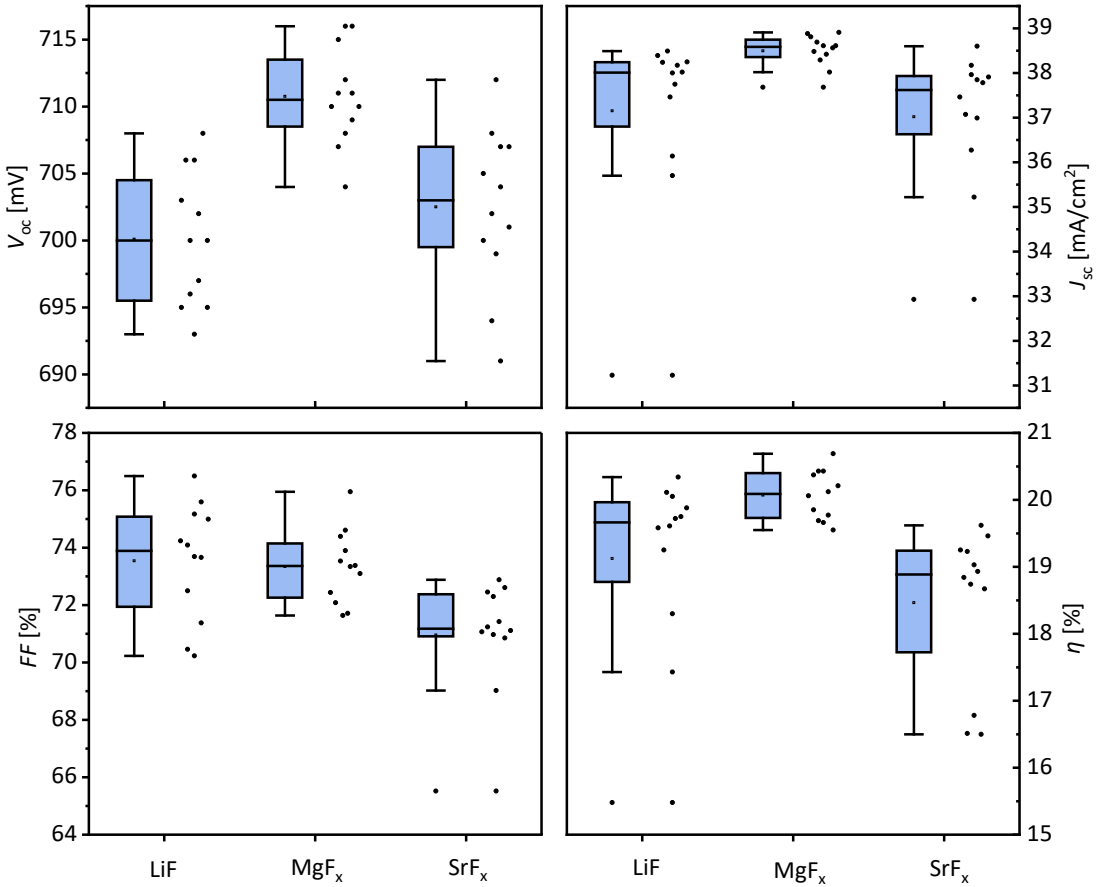

Figure 5.3 External parameters of dopant-free SHJ solar cell integrated of MoO_x on the front and LiF, MgF_x, SrF_x on the rear side

6. Conclusion and outlooks

6.1 Conclusion

The dopant-free SHJ without the doping gases involved in the manufacture process. The CSC as one type of charge carriers selective contact have been paid a large amount attention. The ETL and HTL are worked depending on the materials work function and the deposition method.

The journey into exploring dopant-free materials, specifically to LiF, MgF_x and SrF_x, within SHJ solar cells has been a detailed exploration of materials, interfaces, and their impact on solar cell performance.

Our investigation into different plasma treatments on the LiF/(i)a-Si:H interface has revealed fascinating insights into the performance of SHJ solar cells. We observed that the PTP treatment, involving a highly hydrogen-diluted gas mixture of SiH_4, H_2, and PH_3, provided the highest lifetime among the studied treatments. This indicated superior passivation quality, which is a key factor for efficient solar cells.

Subsequent fabrication of solar cells with different interface treatments demonstrated that PTP-treated cells exhibited the highest V_{oc} and efficiency. The performance was attributed to better surface passivation, as evidenced by the higher lifetime of PTP precursors. The thickness study further revealed that a 1nm LiF layer, in combination with the optimal PTP treatment, maximized the cell efficiency.

Exploring the sequence of LiF and ITO deposition emphasized the importance of LiF protection to (i)a-Si:H. Cell precursors deposited with LiF first exhibited superior performance, emphasizing the role of LiF in protecting the passivation effect from ion bombardment during ITO sputtering process.

Metallization on the rear side introduced considerations for optimal performance. Sputtered Ti/Ag emerged as the preferred combination, providing efficient electron transport while maintaining compatibility with LiF. As for front side metallization methods, copper plating is better than screen printing. Thinner copper-plated fingers have benefit on J_{sc} and *FF,* leading to higher efficiency.

Expanding our exploration to MgF_x, we systematically investigated the optimal thickness of MgF_x layers. The study revealed that a 1nm MgF_x layer provided the highest *FF*, indicating efficient charge transport, while maintaining a balance with overall cell efficiency.

Extending our investigation to SrF_x, the main research on determining the optimal

thickness. The comprehensive study showed that a 4nm layer of SrF_x yielded the highest efficiency. This particular thickness showcased a delicate equilibrium among key factors including V_{oc}, J_{sc}, and *FF*, underlining its potential superiority in enhancing solar cell performance.

In the final stage of our study, we integrated the optimal parameters identified for LiF, MgF_x, and SrF_x into dopant-free SHJ solar cells. Utilizing MoO_x as the HTL on the front side and PTP as the interface treatment on the rear side, we systematically fabricated cells with comparable lifetime levels.

Our findings indicated that MgF_x-based dopant-free cells exhibited the highest efficiency, closely followed by LiF-based cells, and then SrF_x-based cells. This aligns with the individual optimization studies for each material.

In conclusion, this thesis presents a comprehensive exploration of dopant-free materials, providing valuable insights into interface treatments, optimal thicknesses, and the intricate interplay of materials in SHJ solar cells. The roadmap outlined by this research not only advances our understanding of dopant-free technologies but also paves the way for further innovations in the field of solar energy conversion.

6.2 Outlook and Future Directions

From characterization methods aspect, the integration of advanced characterization techniques like X-ray photoelectron spectroscopy (XPS) and Transmission Electron Microscopy (TEM) could be used in the later research. Utilizing XPS could provide insights into the stoichiometry of metal fluorides [78], while TEM could unravel the intricate interface morphology between different plasma-treated surfaces and metal fluorides [79]. These methods are aiming to enrich our understanding of material composition and structure, contributing to enhanced solar cell development.

Consideration the current loss introduced at rear side, a mono-side textured wafers could be employed [74]. The ETL and metal contact deposit on rear side with flat surface might mitigate the parasitic absorption happened in thick metal layer. The pathway could help us achieve higher efficiency.

Exploring the performance difference between n-type wafers and p-type wafers [80], holds significant research value. Additionally, understanding how varying wafer thicknesses influence solar cell efficiency could provide crucial insights into optimization strategies [81].

Acknowledgements

References

[1]   "At 26.81%, LONGi sets a new world record efficiency for silicon solar cells."

[2]   N. Abas, A. Kalair, and N. Khan, "Review of fossil fuels and future energy technologies," *Futures*, vol. 69, pp. 31–49, May 2015, doi: 10.1016/j.futures.2015.03.003.

[3]   N. L. Panwar, S. C. Kaushik, and S. Kothari, "Role of renewable energy sources in environmental protection: A review," *Renewable and Sustainable Energy Reviews*, vol. 15, no. 3. pp. 1513–1524, Apr. 2011. doi: 10.1016/j.rser.2010.11.037.

[4]   A. G. Olabi, "Energy quadrilemma and the future of renewable energy," *Applied Energy*, vol. 108. Elsevier Ltd, pp. 1–6, 2016. doi: 10.1016/j.energy.2016.07.145.

[5]   M. Bollen and F. Hassan, *Integration of Distributed Generation in the Power System*. Wiley, 2011. doi: 10.1002/9781118029039.

[6]   S. Philipps, F. Ise, W. Warmuth, and P. Projects GmbH, "Photovoltaics Report." [Online]. Available: www.ise.fraunhofer.de

[7]   H. Lin *et al.*, "Silicon heterojunction solar cells with up to 26.81% efficiency achieved by electrically optimized nanocrystalline-silicon hole contact layers," *Nat Energy*, vol. 8, no. 8, pp. 789–799, Aug. 2023, doi: 10.1038/s41560-023-01255-2.

[8]   N. Renewable Energy Lab, "NREL Best Research Cell Efficiencies Chart."

[9]   Y. Zhao *et al.*, "Strategies for realizing high-efficiency silicon heterojunction solar cells," *Solar Energy Materials and Solar Cells*, vol. 258, Aug. 2023, doi: 10.1016/j.solmat.2023.112413.

[10]   J. Li *et al.*, "Inter-atomic diffusion of fluorine and oxygen forming electron-selective extraction for high-efficiency dopant-free silicon solar cells," *J Alloys Compd*, vol. 934, Feb. 2023, doi: 10.1016/j.jallcom.2022.167845.

[11]   L. Neusel, M. Bivour, and M. Hermle, "Selectivity issues of MoOx based hole contacts," in *Energy Procedia*, Elsevier Ltd, 2017, pp. 425–434. doi: 10.1016/j.egypro.2017.09.268.

[12]   Z. C. Holman *et al.*, "Current losses at the front of silicon heterojunction solar cells," *IEEE J Photovolt*, vol. 2, no. 1, pp. 7–15, 2012, doi: 10.1109/JPHOTOV.2011.2174967.

[13]   J. Bullock *et al.*, "Efficient silicon solar cells with dopant-free asymmetric heterocontacts," *Nat Energy*, vol. 1, no. 3, Mar. 2016, doi: 10.1038/NENERGY.2015.31.

[14]   Y. Wang, S. T. Zhang, L. Li, X. Yang, L. Lu, and D. Li, "Dopant-free passivating contacts for crystalline silicon solar cells: Progress and prospects," *EcoMat*, vol. 5, no. 2. John Wiley and Sons Inc, Feb. 01, 2023. doi: 10.1002/eom2.12292.

[15]   T. Matsui, M. Bivour, P. Ndione, P. Hettich, and M. Hermle, "Investigation of atomic-layer-deposited TiOx as selective electron and hole contacts to crystalline silicon," in *Energy Procedia*, Elsevier Ltd, 2017, pp. 628–634. doi: 10.1016/j.egypro.2017.09.093.

[16]   J. Geissbühler *et al.*, "22.5% efficient silicon heterojunction solar cell with

molybdenum oxide hole collector."

[17]   J. Bullock *et al.*, "Lithium Fluoride Based Electron Contacts for High Efficiency n-Type Crystalline Silicon Solar Cells," *Adv Energy Mater*, vol. 6, no. 14, Jul. 2016, doi: 10.1002/aenm.201600241.

[18]   Y. Wan *et al.*, "Magnesium Fluoride Electron-Selective Contacts for Crystalline Silicon Solar Cells," *ACS Appl Mater Interfaces*, vol. 8, no. 23, pp. 14671–14677, Jun. 2016, doi: 10.1021/acsami.6b03599.

[19]   J. Dréon *et al.*, "23.5%-efficient silicon heterojunction silicon solar cell using molybdenum oxide as hole-selective contact," *Nano Energy*, vol. 70, Apr. 2020, doi: 10.1016/j.nanoen.2020.104495.

[20]   L. Cao *et al.*, "Achieving 23.83% conversion efficiency in silicon heterojunction solar cell with ultra-thin MoOx hole collector layer via tailoring (i)a-Si:H/MoOx interface," *Progress in Photovoltaics: Research and Applications*, 2022, doi: 10.1002/pip.3638.

[21]   W. Wang *et al.*, "Stable Dopant-Free Electron-Selective Contact for Silicon Solar Cells," *ACS Appl Energy Mater*, vol. 6, no. 21, pp. 11234–11241, Nov. 2023, doi: 10.1021/acsaem.3c02133.

[22]   X. Yang, Q. Bi, H. Ali, K. Davis, W. V. Schoenfeld, and K. Weber, "High-Performance TiO2-Based Electron-Selective Contacts for Crystalline Silicon Solar Cells," *Advanced Materials*, vol. 28, no. 28, pp. 5891–5897, Jul. 2016, doi: 10.1002/adma.201600926.

[23]   X. Yang, P. Zheng, Q. Bi, and K. Weber, "Silicon heterojunction solar cells with electron selective TiOx contact," *Solar Energy Materials and Solar Cells*, vol. 150, pp. 32–38, Jun. 2016, doi: 10.1016/j.solmat.2016.01.020.

[24]   J. Cho *et al.*, "Passivating electron-selective contacts for silicon solar cells based on an a-Si:H/TiOx stack and a low work function metal," *Progress in Photovoltaics: Research and Applications*, vol. 26, no. 10, pp. 835–845, Oct. 2018, doi: 10.1002/pip.3023.

[25]   J. Bullock *et al.*, "Dopant-Free Partial Rear Contacts Enabling 23% Silicon Solar Cells," *Adv Energy Mater*, vol. 9, no. 9, Mar. 2019, doi: 10.1002/aenm.201803367.

[26]   J. Cho *et al.*, "Performance and Thermal Stability of an a-Si:H/TiOx/Yb Stack as an Electron-Selective Contact in Silicon Heterojunction Solar Cells," *ACS Appl Energy Mater*, vol. 2, no. 2, pp. 1393–1404, Feb. 2019, doi: 10.1021/acsaem.8b01969.

[27]   "Silicon - Electronics, Solar Cells, Alloys _ Britannica".

[28]   D. Gray, A. Mccaughan, and B. Mookerji, "Crystal Structure of Graphite, Graphene and Silicon," 2009. [Online]. Available: http://physics.nist.gov/PhysRefData/.

[29]   J. J. Low, M. L. Kreider, D. P. Pulsifer, A. S. Jones, and T. H. Gilani, "Band Gap Energy in Silicon."

[30]   T. Zhang and H. Yang, "High efficiency plants and building integrated renewable

energy systems: Building-integrated photovoltaics (BIPV)," in *Handbook of Energy Efficiency in Buildings: A Life Cycle Approach*, Elsevier, 2018, pp. 441–595. doi: 10.1016/B978-0-12-812817-6.00040-1.

[31]   J. A. Röhr, "Electron Transport in Solution Processed Antimony Sulphide Thin Films made from a Xanthate Precursor," 2014.

[32]   S. De Wolf, A. Descoeudres, Z. C. Holman, and C. Ballif, "High-efficiency silicon heterojunction solar cells: A review," *green*, vol. 2, no. 1, pp. 7–24, 2012.

[33]   P. Procel *et al.*, "The role of heterointerfaces and subgap energy states on transport mechanisms in silicon heterojunction solar cells," *Progress in Photovoltaics: Research and Applications*, vol. 28, no. 9, pp. 935–945, Sep. 2020, doi: 10.1002/pip.3300.

[34]   Z. Sun *et al.*, "Toward Efficiency Limits of Crystalline Silicon Solar Cells: Recent Progress in High-Efficiency Silicon Heterojunction Solar Cells," *Advanced Energy Materials*, vol. 12, no. 23. John Wiley and Sons Inc, Jun. 01, 2022. doi: 10.1002/aenm.202200015.

[35]   M. F. Abdullah *et al.*, "Research and development efforts on texturization to reduce the optical losses at front surface of silicon solar cell," *Renewable and Sustainable Energy Reviews*, vol. 66. Elsevier Ltd, pp. 380–398, Dec. 01, 2016. doi: 10.1016/j.rser.2016.07.065.

[36]   A. Fell *et al.*, "Modeling parasitic absorption in silicon solar cells with a near-surface absorption parameter," *Solar Energy Materials and Solar Cells*, vol. 236, Mar. 2022, doi: 10.1016/j.solmat.2021.111534.

[37]   A. Wang and Y. Xuan, "A detailed study on loss processes in solar cells," *Energy*, vol. 144, pp. 490–500, Feb. 2018, doi: 10.1016/j.energy.2017.12.058.

[38]   A. Smets, K. Jäger, O. Isabella, R. Van Swaaij, and M. Zeman, *Solar Energy: The physics and engineering of photovoltaic conversion, technologies and systems*. Bloomsbury Publishing, 2016.

[39]   F. Verlag, "ANALYSIS OF PHOTONIC STRUCTURES FOR SILICON SOLAR CELLS." [Online]. Available: www.ise.fraunhofer.de

[40]   W. Siiocklev and A. W. T. Read, "A SOLUBLE PROBLEM IN ENERGY HANDS Statistics of the Recombinations of Holes and Electrons," 1952.

[41]   G. Yang *et al.*, "Oxygen-alloyed poly-Si passivating contacts for high-thermal budget c-Si heterojunction solar cells," *Progress in Photovoltaics: Research and Applications*, vol. 30, no. 2, pp. 141–151, Feb. 2022, doi: 10.1002/pip.3472.

[42]   "Pavel_Babal_PhD_thesis".

[43]   A. Bashir, T. I. Awan, A. Tehseen, M. B. Tahir, and M. Ijaz, "Interfaces and surfaces," in *Chemistry of Nanomaterials: Fundamentals and Applications*, Elsevier, 2020, pp. 51–87. doi: 10.1016/B978-0-12-818908-5.00003-2.

[44]   "Deposition."

[45]   C. Han *et al.*, "Room-temperature sputtered tungsten-doped indium oxide for improved current in silicon heterojunction solar cells," *Solar Energy Materials and Solar Cells*, vol. 227, Aug. 2021, doi: 10.1016/j.solmat.2021.111082.

[46] G. Yang, "High-efficient n-i-p thin-film silicon solar cells."

[47] M. C. Raval and S. Madugula Reddy, *Industrial Silicon Solar Cells*. IntechOpen, 2020. doi: 10.5772/intechopen.84817.

[48] "The flow chart of photolithography."

[49] "electrolytic plating."

[50] "M-2000 ®."

[51] V. M. Airaksinen, "Silicon Wafer and Thin Film Measurements," in *Handbook of Silicon Based MEMS Materials and Technologies: Second Edition*, Elsevier Inc., 2015, pp. 381–390. doi: 10.1016/B978-0-323-29965-7.00015-4.

[52] "UV/Vis/NIR From Your Perspective."

[53] O. Hamdy and H. S. Mohammed, "Investigating the transmission profiles of 808 nm laser through different regions of the rat's head", doi: 10.1007/s10103-020-03098-9/Published.

[54] N. Ewen Grant and A. National, "Surface passivation and characterisation of crystalline silicon by wet chemical treatments," 2012.

[55] "I-V Characteristics of a Solar Cell."

[56] A. , J. K. , I. O. , V. S. R. , & Z. M. Smets, *Solar Energy: The physics and engineering of photovoltaic conversion, technologies and systems.* . 2016.

[57] S. E. Shaheen, C. J. Brabec, N. S. Sariciftci, F. Padinger, T. Fromherz, and J. C. Hummelen, "2.5% efficient organic plastic solar cells," *Appl Phys Lett*, vol. 78, no. 6, pp. 841–843, Feb. 2001, doi: 10.1063/1.1345834.

[58] B. N. Taylor, "The International System of Units (SI)," 2001.

[59] "Pseudo Light I-V Curve Without the EEect of Rs Suns-Voc MX: Post-Diffusion Process Control Product Overview Industry Leading Technology for Silicon PV Process Control," 2022. [Online]. Available: www.sintoninstruments.com

[60] N. J. Shivaramu, B. N. Lakshminarasappa, E. Coetsee, and H. C. Swart, "Chapter 9 - Thermoluminescent materials for high-energy dosimetry," in *Radiation Dosimetry Phosphors*, S. Dhoble, V. Chopra, V. Nayar, G. Kitis, D. Poelman, and H. Swart, Eds., in Woodhead Publishing Series in Electronic and Optical Materials. , Woodhead Publishing, 2022, pp. 211–251. doi: https://doi.org/10.1016/B978-0-323-85471-9.00002-6.

[61] "Production details of LiF."

[62] "Production details of magnesium fluoride."

[63] K. Suzuki, M. Cadatal-Raduban, M. Kase, and S. Ono, "Band gap engineering of CaxSr1-xF2 and its application as filterless vacuum ultraviolet photodetectors with controllable spectral responses," *Opt Mater (Amst)*, vol. 88, pp. 576–579, 2019, doi: https://doi.org/10.1016/j.optmat.2018.12.023.

[64] "document".

[65] L. Sims *et al.*, "Investigation of the s-shape caused by the hole selective layer in bulk heterojunction solar cells," *Org Electron*, vol. 15, no. 11, pp. 2862–2867, 2014, doi: 10.1016/j.orgel.2014.08.010.

[66] J. Bullock *et al.*, "Efficient silicon solar cells with dopant-free asymmetric

heterocontacts," *Nat Energy*, vol. 1, no. 3, Mar. 2016, doi: 10.1038/NENERGY.2015.31.

[67] C. Han *et al.*, "High-Mobility Hydrogenated Fluorine-Doped Indium Oxide Film for Passivating Contacts c-Si Solar Cells," *ACS Appl Mater Interfaces*, vol. 11, no. 49, pp. 45586–45595, Dec. 2019, doi: 10.1021/acsami.9b14709.

[68] X. Yang *et al.*, "Tantalum Nitride Electron-Selective Contact for Crystalline Silicon Solar Cells," *Adv Energy Mater*, vol. 8, no. 20, Jul. 2018, doi: 10.1002/aenm.201800608.

[69] W. Zheng *et al.*, "Defect-Free Metal Deposition on 2D Materials via Inkjet Printing Technology," *Advanced Materials*, vol. 34, no. 48, Dec. 2022, doi: 10.1002/adma.202104138.

[70] J. Yu *et al.*, "Copper metallization of electrodes for silicon heterojunction solar cells: Process, reliability and challenges," *Solar Energy Materials and Solar Cells*, vol. 224. Elsevier B.V., Jun. 01, 2021. doi: 10.1016/j.solmat.2021.110993.

[71] C. Han *et al.*, "Controllable Simultaneous Bifacial Cu-Plating for High-Efficiency Crystalline Silicon Solar Cells," *Solar RRL*, vol. 6, no. 6, Jun. 2022, doi: 10.1002/solr.202100810.

[72] Y. Wan *et al.*, "Magnesium Fluoride Electron-Selective Contacts for Crystalline Silicon Solar Cells," *ACS Appl Mater Interfaces*, vol. 8, no. 23, pp. 14671–14677, Jun. 2016, doi: 10.1021/acsami.6b03599.

[73] W. Wu *et al.*, "22% efficient dopant-free interdigitated back contact silicon solar cells," in *AIP Conference Proceedings*, American Institute of Physics Inc., Aug. 2018. doi: 10.1063/1.5049288.

[74] Y. Wan *et al.*, "Magnesium Fluoride Electron-Selective Contacts for Crystalline Silicon Solar Cells," *ACS Appl Mater Interfaces*, vol. 8, no. 23, pp. 14671–14677, Jun. 2016, doi: 10.1021/acsami.6b03599.

[75] C. Xing *et al.*, "SrFx-based electron-selective contact with high tolerance to thickness for crystalline silicon solar cells enabling efficiency over 21%," *Progress in Photovoltaics: Research and Applications*, 2023, doi: 10.1002/pip.3733.

[76] W. Wang *et al.*, "Stable Dopant-Free Electron-Selective Contact for Silicon Solar Cells," *ACS Appl Energy Mater*, vol. 6, no. 21, pp. 11234–11241, Nov. 2023, doi: 10.1021/acsaem.3c02133.

[77] N. Chen *et al.*, "Gadolinium Fluoride as a High-Thickness-Tolerant Electron-Selective Contact Material for Solar Cells," *ACS Appl Energy Mater*, vol. 5, no. 4, pp. 4351–4357, Apr. 2022, doi: 10.1021/acsaem.1c03919.

[78] S. Cao *et al.*, "Stable MoOX-Based Heterocontacts for p-Type Crystalline Silicon Solar Cells Achieving 20% Efficiency," *Adv Funct Mater*, vol. 30, no. 49, Dec. 2020, doi: 10.1002/adfm.202004367.

[79] Z. Liu *et al.*, "Tailoring protective metals for high-efficient and stable dopant-free crystalline silicon solar cells," *Solar Energy Materials and Solar Cells*, vol. 256, Jul. 2023, doi: 10.1016/j.solmat.2023.112343.

[80] T. G. Allen, J. Bullock, X. Yang, A. Javey, and S. De Wolf, "Passivating contacts for

crystalline silicon solar cells," *Nature Energy*, vol. 4, no. 11. Nature Publishing Group, pp. 914–928, Nov. 01, 2019. doi: 10.1038/s41560-019-0463-6.

[81] H. Dai, L. Yang, and S. He, "< 50-µm thin crystalline silicon heterojunction solar cells with dopant-free carrier-selective contacts," *Nano Energy*, vol. 64, Oct. 2019, doi: 10.1016/j.nanoen.2019.103930.

Appendix

A1

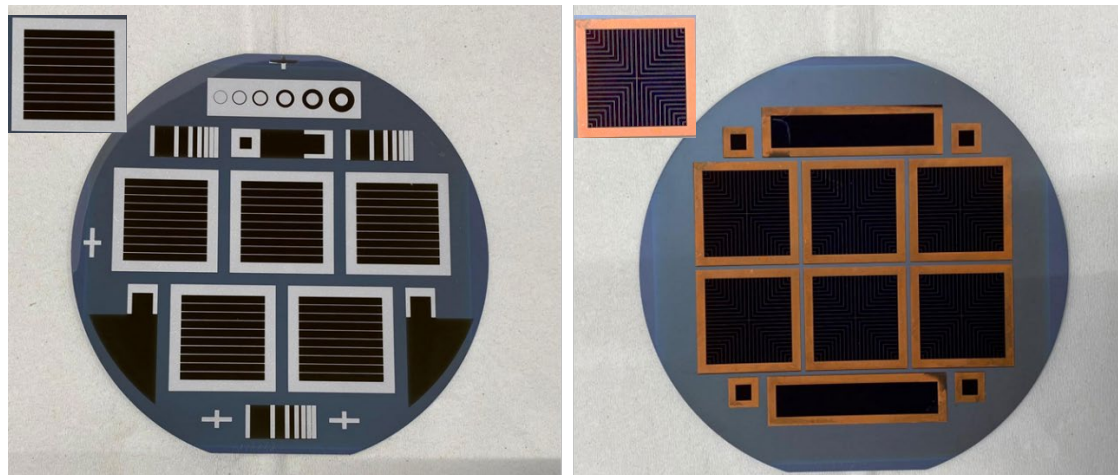The appearance of screen printing (SP) sample and copper plating (CP) sample.

Figure A1. The outlook of screen printing and copper plating cell

A2

The optical parameters of ETL materials are given in Table A2.

Table A2. The *n,k* values and transmittance of ETL from previous studies

Materials	n	k	T (at 1nm thickness)
LiF	1.3921		
MgF$_2$	1.4220	0.00058239	0.99999
SrF$_2$	1.4868	0.0070393	0.99985

*n value at wavelength of 583.6nm

A3

The surface distribution of the thin ETL layer is assessed using Spectroscopic Ellipsometry (SE). Samples for uniform deposition are taken from the same batch of cell precursors. The thin layer is deposited onto Corning glass, divided into nine squares to facilitate thickness measurements, as illustrated in Figure A3.
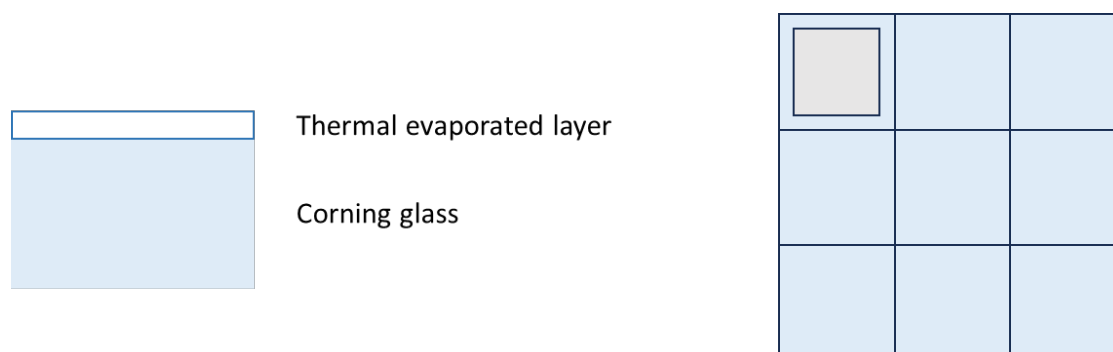

Thermal evaporated layer

Corning glass

Figure A3. The sketch of uniformity of ETL thin layer

50

A4
Champion cell with IWO

The champion cell within 1nm LiF is broken by accident. But considering from efficiency point of view, 3nm LiF cell with other optimal parameters has the highest efficiency with structure as given in Figure A4.
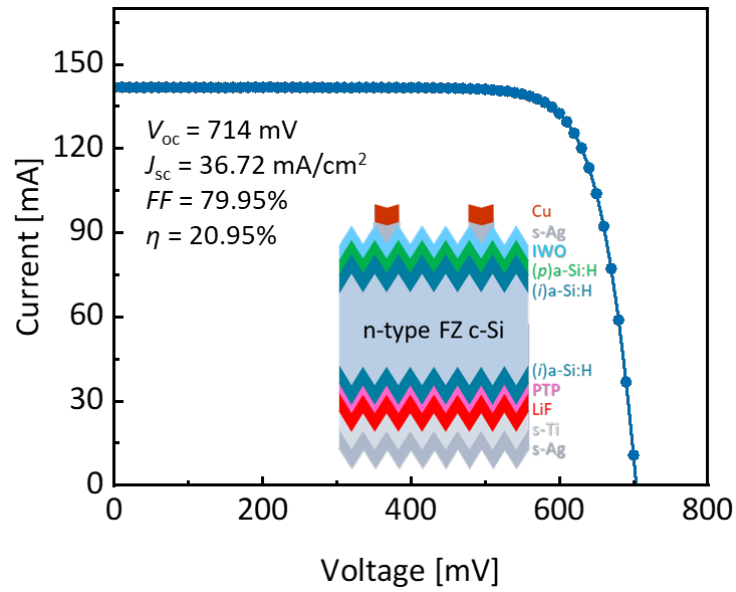

Figure A4. The *I-V* curve and schematic of champion cell

A5
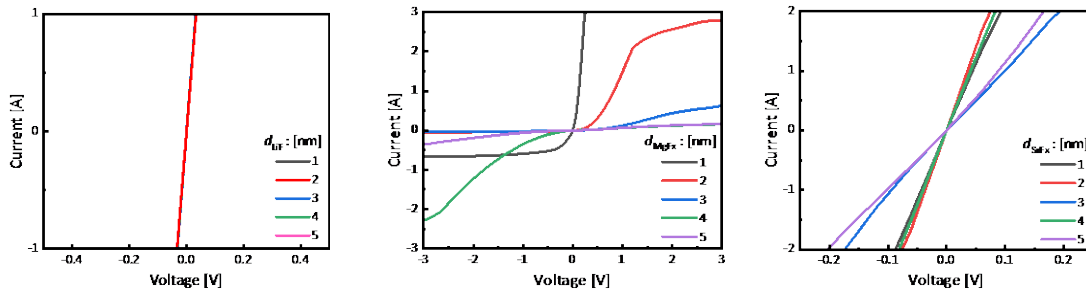The contact resistivity of LiF, MgF$_x$ and SrF$_x$ are given in Figure A5.

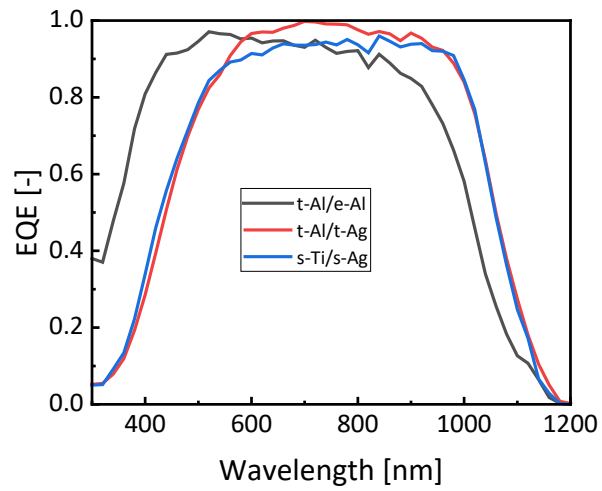Figure A5. The contact resistivity of LiF, MgF$_x$ and SrF$_x$

A6

Figure A6. The EQE of SHJ solar cells with different rear side metal contacts

A7

The difference between *FF* and *pFF*.

Table A7. The difference between *FF* and *pFF*

Sample	*FF*	*pFF*	*pFF - FF*
	[%]	[%]	[%]
M18572	77.49	85.70	8.21
M18614	77.93	80.8	2.87
M18616	75.17	85.3	10.13